Engineering Structures 225 (2020) 111257

Contents lists available at ScienceDirect

Engineering Structures

journal homepage: www.elsevier.com/locate/engstruct

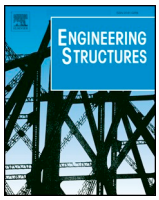

# Seismic performance of slender RC U-shaped walls with a single-layer of reinforcement

Ryan Hoult[a,*], Aaron Appelle[a], João Almeida[b], Katrin Beyer[a]

[a] École Polytechnique Fédérale de Lausanne, Earthquake Engineering and Structural Dynamics, Lausanne, Switzerland
[b] Institute of Mechanics, Materials and Civil Engineering, UCLouvain, Louvain-la-Neuve, Belgium

A B S T R A C T

Reinforced concrete walls are commonly used to resist the lateral loading induced by wind and earthquake actions. While most walls include two vertical reinforcement layers, some regions of the world construct slender, non-rectangular concrete walls with a single vertical layer of reinforcement. The seismic performance of such elements is largely unknown given the paucity of experimental research. This paper presents the results of two slender reinforced concrete U-shaped walls tested at the Earthquake Engineering and Structural Dynamics Laboratory (EESD Lab), École Polytechnique Fédérale de Lausanne (EPFL) in Switzerland. Both wall specimens, designed similar to construction practice in Colombia, were tested using quasi-static cyclic loading to observe if out-of-plane instability would develop when deformations were limited to prevent the flange boundary ends crushing. Initial failure of both wall specimens corresponded with local out-of-plane buckling in the boundary ends of the flanges occurring on load reversal. The buckling lengths were approximately 700–800 mm, which corresponded to 44–50 bar diameters. The crack patterns were observed to be steepest in the web of the walls, demonstrating the increased shear demand in comparison to that of a rectangular wall. Both wall specimens reached ultimate drifts larger than 2.5–3.0% before global failure occurring in the web-flange intersection due to crushing. A small twist was subjected to one of the walls when centered and loaded diagonally, which showed that the decay in torsional stiffness is proportional to the decay in translational stiffness.

## 1. Introduction

Reinforced Concrete (RC) walls are commonly used as the primary lateral force-resisting elements in RC buildings, where core walls resist wind and earthquake loading in both horizontal directions. There has recently been a proliferation of mid- to high-rise RC shear wall buildings in several Latin American countries. Due to some loopholes in the current material standards in some countries (e.g. Colombia), it is anticipated that many of the RC walls embedded in these buildings are slender (80 – 100 mm), unconfined, and detailed with a single-layer of vertical reinforcement [14,50,13,12,33]. For example, no special transverse reinforcement to confine the boundary ends of RC walls is required by some building codes in Latin American [38]. Furthermore, a minimum longitudinal reinforcement ratio ($\rho_{wv}$) of just 0.25% is required by the building codes in Colombia for RC walls [4], which is low considering the amount typically required to cause secondary cracking and ensure that a ductile response of the wall is achieved in the event of an earthquake [29,30,36]. However, concentrating reinforcement in the boundary ends of the wall is also practiced in Latin America if higher flexural demands are required [13]. RC walls (or cores) are often non-rectangular due to architectural and structural requirements [6,51,13]. The U-shaped wall is among the simplest non-rectangular walls yet illustrates many differences to rectangular walls [7]. Firstly, the behavior of U-shaped walls differs from rectangular walls with regards to the lateral strength and stiffness of the wall [43]. U-shaped walls also have three primary in-plane modes of bending in comparison to rectangular walls, which only have one; a U-shaped wall can bend about its major (strong) axis and about its minor (weak) axis with web-in-compression and web-in-tension. Furthermore, the diagonal loading direction in U-shaped walls has been identified as potentially the most critical loading direction [18], primarily due to the complexity of distributing shear forces to the different wall sections [34]and the loading direction that corresponds to the lowest in-plane displacement capacities [8]. In regions of low seismicity, RC U-shaped walls are often placed on the perimeter of buildings to make more efficient use of the building area, which creates asymmetry in-plan due to the distribution of stiffness and strength [45,27,46]. This type of building configuration has the potential to twist and cause torsional actions to a U-shaped wall when subjected to earthquake ground motions. Even in high seismic regions, RC U-shaped walls have the potential to be subjected to some twisting actions in the event of an earthquake [32]. To summarize, in comparison to planar (rectangular) RC walls, non-planar wall sections, such as the U-shaped wall, are more likely to be subjected to multiple loading directions in the event of an earthquake, including some torsional actions.

Given that Colombia includes regions of high seismicity, RC

* Corresponding author.
*E-mail address:* ryan.hoult@unimelb.edu.au (R. Hoult).

https://doi.org/10.1016/j.engstruct.2020.111257
Received 30 January 2020; Received in revised form 2 July 2020; Accepted 21 August 2020

buildings therein are at risk to experiencing a moderate-to-large earthquake event within the lifetime of the structure. Many of these buildings contain slender and unconfined RC walls with a single layer of longitudinal reinforcement, as discussed above. The seismic performance of these types of structural elements is largely unknown and hard to quantify due to the paucity of experimental research in this area; to the authors' knowledge, there are only relatively few experimental programs that have focused on RC walls with a single layer of reinforcement: Albidah [1] and Altheeb [3] tested (in total) three unconfined rectangular RC walls detailed with a single layer of horizontal and vertical reinforcement, typical of the construction practice in Australia; Puranam and Pujol [47] tested four rectangular RC walls with a single layer of conventional-strength and high-strength longitudinal reinforcing bars to investigate the minimum amount required to ensure that fracturing of the bars did not limit the displacement capacity of the walls; Almeida et al. [2] tested two RC T-shaped walls with a single-layer of reinforcement, corresponding to the current design practices in Colombia; four slender RC T-shaped specimens designed to current Colombian practice were tested by Blandón et al. [13]; more recently, Blandón and Bonett [12] tested two unconfined rectangular RC walls with a single layer of reinforcement, the specimens of which were designed to typical construction practice in moderate seismic regions in South America. In comparison to experimental tests on rectangular RC walls, there is a paucity of experimental research on the seismic performance of U-shaped walls [11]. More recently, the seismic performance of U-shaped or C-shaped walls with two-layers of longitudinal reinforcement has received more attention and several test campaigns have been completed [5,8,11,18,34]. However, all of these walls were designed and tested to achieve high ductilities (i.e., the walls were heavily reinforced and confined). Thus, to the authors' knowledge, there has been no experimental testing to determine the seismic performance of slender RC U-shaped walls with a single-layer of vertical reinforcement.

Despite decades of building design code advancements internationally, earthquake events still allude to unexpected failure mechanisms in RC walls. One of the most recent failure modes corresponded to out-of-plane buckling failures in ductile RC walls observed after the Christchurch, New Zealand earthquake in 2011 [52]and Maule, Chile earthquake in 2010[37]. While this type of failure had been previously reported experimentally [24,41,53], this was the first time it had been widely observed after earthquake events. Correspondingly, there has recently been a great deal of experimental and numerical investigative research focusing on the out-of-plane instability of RC walls due to in-plane loading [20,25,42,49,50]. However, all of these recently tested specimens were either planar (i.e., rectangular) walls or idealized boundary elements. An exception to this is the experimental research by Almedia *et al.* (2017) and Blandon *et al.* (2018), where thin and lightly reinforced T-shaped walls were tested. Yet, the largest ratio of the length of the flange to the length of the web of these specimens was 0.17. Thus, there has yet to be experimental research focusing on the out-of-plane instability of non-planar walls with large, flanged sections, such as U-shaped walls. Thomsen and Wallace [53] suggest that the potential for out-of-plane instability of walls can be exacerbated for the in-plane bending of non-planar sections. Furthermore, unlike the ductile RC walls that were observed to fail due to out-of-plane instability in recent earthquake events, RC walls detailed with a single-layer of reinforcement, which is the current construction practice in some Latin American countries, can also aggravate the potential for this type of failure mode [44]. There are also two types of out-of-plane responses of structural walls that need to be established: local and global instability. As thoroughly discussed in Dashti et al. [21], a summary of the key differences between the two out-of-plane response is given below:

- A large height of the wall (i.e., approximately 70% of the unsupported height) is involved in the formation of global instability, whereas local instability generally corresponds to out-of-plane deformation over a limited height from the wall base.
- An abrupt drop in strength typically corresponds with the final global instability of the wall, whereas very gradual strength degradations are observed with local instability.
- A uniform distribution of cracks (and correspondingly of tensile strains) up the wall height is needed for global instability, whereas local instability generally coincides with larger crack widths expected in fewer cracks in the base region of the wall.

To investigate the seismic performance of slender RC U-shaped walls with a single-layer of reinforcement, an experimental program was conducted at the *Earthquake Engineering and Structural Dynamics Laboratory (EESD Lab)*, *École Polytechnique Fédérale de Lausanne (EPFL)*, Switzerland, testing two full-scale RC U-shaped wall specimens. The work is part of a larger research program in collaboration with three Colombian universities: Universidad EIA, Universidad del Norte and Universidad de Medellín.

## 2. Experimental setup and loading procedure

### 2.1. Geometry of the test units

The two U-shaped walls tested as part of this experimental project had the same cross-sectional dimensions as the test units TUB [8], TUC and TUD [18]. Both units tested here, denoted TUE (Test Unit E) and TUF (Test Unit F), were full-scale models of the lower three storeys of an idealized core that could enclose a small elevator. While there may be some interaction between the diaphragm and the wall at each interstorey height in a real structure, the test setup used here is limited to assuming cantilever-wall conditions without that interaction. Blandón and Bonett [12] found that the mean axial load ratio (*ALR*) from fourteen buildings between 6 and 12 stories in Colombia was 6.9%. Furthermore, Arteta et al. [4] studied twenty-eight multistory thin-walled RC buildings from Colombia and found the *ALR* was positively correlated with height of the walls and can be approximated as $ALR \approx H_w/500$, where $H_w$ is the full height of the wall (in metres); for the walls tested here (Fig. 1b), this would correspond to an *ALR* of approximately 0.93%, which is negligible. One of the primary focuses of this study was to observe if out-of-plane instability was a problem for these types of walls. As such, no axial load was applied on either specimen to reduce the potential for an unconfined concrete crushing-type failure. The reinforcement content for the two test specimens is given in Table 1, which conforms with typical Colombian construction practice as discussed previously. The lumped longitudinal reinforcement in the boundary regions in the wall (Fig. 1a) is common practice in Colombia for when higher flexural demands are required (Blandon *et al.*, 2018), and the larger reinforcement content in these areas of the wall have been shown to be more prone to out-of-plane instability [50]. While the reinforcement layout was identical in both walls (shown in Fig. 1a), the loading protocol differed for each wall, as discussed in Section 2.4.

### 2.2. Material properties

The aim was for a design compressive strength of the concrete at 28-days ($f'_c$) of 30 MPa for the walls, as typical concrete strengths in Colombia construction was found to range from 21 MPa to 35 MPa (Mejia *et al.*, 2004). The expressions from Paulay and Priestley [44] and Chai and Elayer [16] also indicate that a lower compressive strength results in a wall that is more susceptible to out-of-plane instability. The concrete compressive strength ($f_c$) and tensile strength ($f_t$) of the two test specimens are given in Table 2. All properties were obtained from material tests on the day of testing each unit.

The yield strength ($f_y$), the ultimate strength ($f_u$), Young's modulus ($E_s$) and the ultimate strain ($\varepsilon_{su}$) of the reinforcing bars for both TUE and TUF are given in Table 3. Furthermore, for the D16 bars used in the

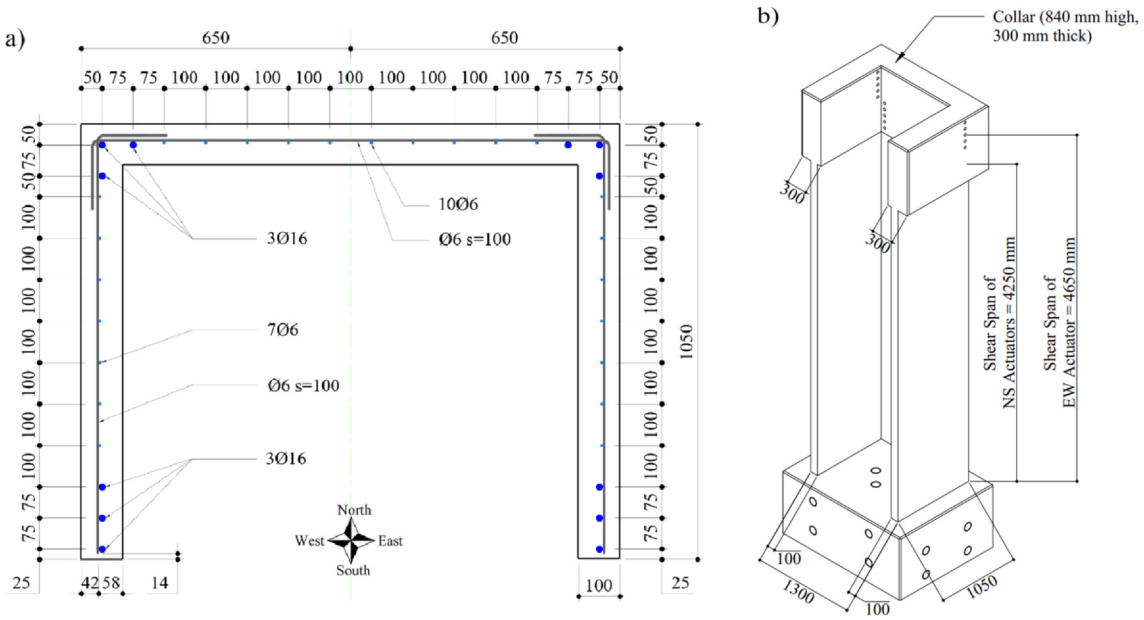


**Fig. 1.** Test units TUE and TUF: (a) cross-section and reinforcement layout and (b) elevation view (not to scale; dimensions in mm).

**Table 1**
U-shaped wall parameters for test units TUE and TUF.

| | TUE/TUF |
|---|---|
| Shear Span ($M$ / $V$ = $H_e$) | 4.25m[a] / 4.65m[b] |
| Shear Span Ratio ($H_e$ / $L_w$[c]) | 4.05[a] / 3.58[b] |
| Axial Load Ratio ($P/f_cA_g$) | 0.00 |
| Lumped Vertical Reinforcement Ratio ($\rho_{be}$) | 3.02% |
| Distributed Vertical Reinforcement Ratio ($\rho_{wv}$) | 0.30% |
| Horizontal Reinforcement Ratio ($\rho_{wh}$) | 0.28% |

[a] for displacements parallel to the flanges (NS direction), about its minor axis
[b] for displacements parallel to the web (EW direction), about its major axis
[c] the wall length ($L_w$) corresponds to the wall component parallel to the direction of loading

**Table 2**
Mechanical properties of the concrete for TUE and TUF.

| | Compression Tests | | Tension Tests | |
|---|---|---|---|---|
| | $f_c$ (MPa) | No. of samples | $f_t$ (MPa) | No. of samples |
| TUE | 31.7 | 4 | 2.1 | 4 |
| TUF | 28.7 | 6 | 2.7 | 4 |

**Table 3**
Mechanical properties of the reinforcing steel for TUE and TUF.

| | $f_y$ (MPa) | $f_u$ (MPa) | $f_u$ / $f_y$ | $E_s$ (MPa) | $\varepsilon_{sh}$ | $\varepsilon_{su}$ |
|---|---|---|---|---|---|---|
| D6 | 475 | 625 | 1.32 | 204,000 | – | 0.098 |
| D16 (TUE) | 521 | 627 | 1.20 | 193,186 | 0.0160 | 0.121 |
| D16 (TUF) | 523 | 637 | 1.22 | 183,114 | 0.0077 | 0.083 |

boundary ends of the wall, the strain at onset of strain hardening ($\varepsilon_{sh}$) is given. As indicated by the $f_u$ / $f_y$ values in Table 3, the D16 and D6 bars used in the wall correspond to "Class C" (i.e., ductile), according to Eurocode 8 [15].

### 2.3. Test setup and instrumentation

A photo of specimen TUE and the test setup is shown in Fig. 2a. Similar to the tests conducted by Beyer et al. [8] and Constantin and Beyer [18], the walls were loaded horizontally with three actuators: the east–west (EW) actuator loaded the web of the wall at a height ($h_{EW}$) of 4.65 m, while the north–south (NS) actuators loaded the flanges of the wall at a height ($h_{NS}$ of 4.25 m. The tests were performed in displacement control; details on the loading protocol and the applied boundary conditions are given in Section 2.4.

#### 2.3.1. Conventional instrumentation

Throughout testing the wall behavior was monitored with conventional instrumentation, i.e. linear variable differential transducers (LVDTs) and load cells. Photos, hand notes and some manual measurements of cracks were collected during testing, which will be made publicly available (see Section 6). The layout of the measurement systems is shown in Fig. 2b. The LVDTs were used to measure the global horizontal (in-plane) displacements at the collar (top of the wall).

#### 2.3.2. Optical triangulation measurements

The three-dimensional displacement field of the surface ends of the flanges (i.e., boundary ends to the South) of each wall was measured by a grid of infrared light-emitting diodes (LEDs) with a recording frequency of 5 Hz. The position of each LED was tracked by a camera consisting of three digital optical sensors. The software and hardware used was a commercial system provided by NDI Optotrak Certus HD [40]. Similar to the methods used in Almeida et al. [2], two cameras were used to improve the accuracy, each covering approximately half the wall height. 120 LEDs were used to track the displacements of the flange ends of both TUE and TUF. The LEDs were glued on the faces of the flange ends in vertical increments of 100 mm to match the horizontal reinforcement spacing. Three LEDs were used across the thickness of the wall, which were spaced 30 mm apart (and 20 mm in from the wall edge). The LEDs are used to track the displacement profile. From these displacements, among others, the out-of-plane displacement profiles of the flanges, the strains at the flange ends as well as the strain variation across the thickness of the wall can be computed throughout testing. Furthermore, to check that foundation displacements remained negligible during testing, LEDs were attached to small L-shaped steel brackets on the foundation. The LED coordinates were transformed during the data post-processing stage: the origin of the coordinate system is at the center of the web and is illustrated in Fig. 3 with corresponding positive coordinate directions; the x-axis refers to the horizontal in-plane direction of the wall parallel to the web (positive

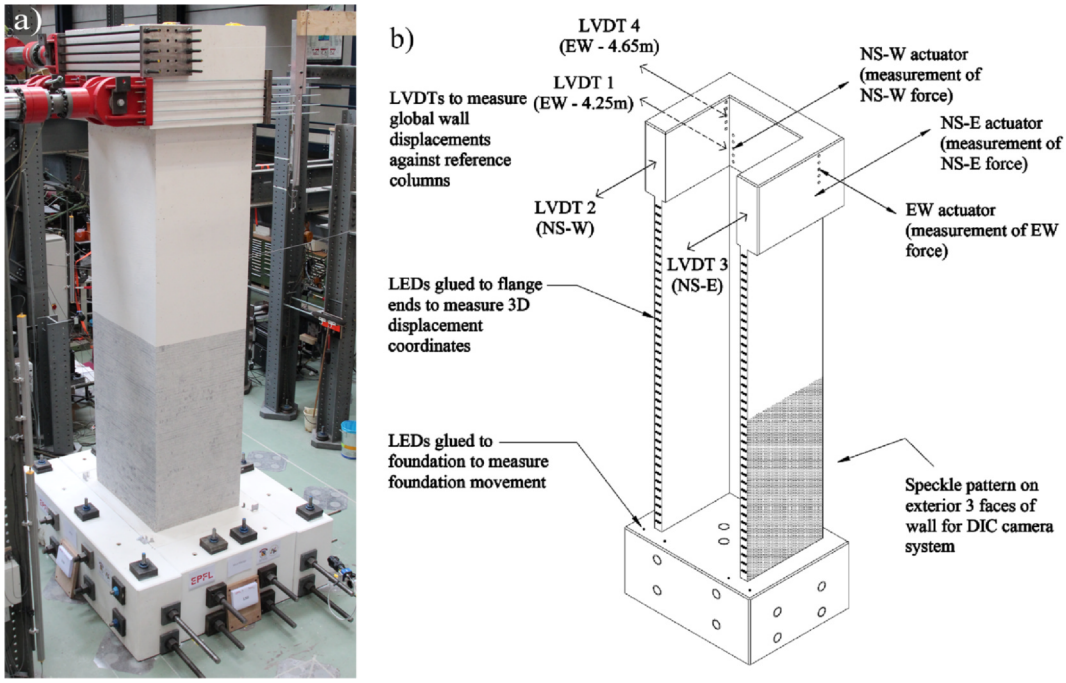


**Fig. 2.** (a) Test setup of TUE and (b) location of conventional and optical measurement devices (dimensions in mm).

direction from center of web to the east flange); the y-axis refers to the vertical in-plane direction (positive direction from foundation to collar, or bottom to top); the z-axis refers to the horizontal in-plane direction of the wall parallel to the flanges (positive direction from the center of web to boundary ends of the flanges).

### 2.3.3. Digital image correlation measurements

A speckle pattern for digital image correlation (DIC) measurements was applied on three outside surfaces of the wall (East flange, web and West flange) covering a height from the base of approximately 2 m. The speckle pattern was applied by a stencil with a computer-generated random pattern to produce black dots with an approximate diameter of 5 mm. As each wall was either subjected to bidirectional or diagonal loading, 3-D DIC systems were used. Thus, for each unit, 3 sets of two 3-D Manta camera systems were used, each set capturing a different section of the wall. The Manta cameras recorded black and white photographs to decrease file size and simultaneously have an increased capacity for sensor dimensions, resulting in high resolution images. The DIC systems recorded images of the wall segments at a frequency of 0.05 Hz (i.e., every 20 s).

## 2.4. Loading protocol

The experimental research here is a continuation of previous experimental programs focusing on the seismic performance of RC U-shaped walls. Beyer et al. [8] subjected two RC U-shaped wall specimens (TUA and TUB) to loading in five different directions, including a "sweep" and a diagonal loading direction, which was based on a loading pattern developed by Hines et al. [26] for reinforced concrete bridge piers. Furthermore, a small twist was applied to specimens TUA and TUB at different in-plane flexural positions to investiagte the decay of torsional stiffness. Constantin and Beyer [18] tested two RC U-shaped walls (TUC and TUD) with loading primarily being applied along the two geometric diagonals of the sections, as the key objective was to understand the behaviour of the wall under diagonal loading.

As outlined in Section 2.1, specimens TUE and TUF had the same geometry and reinforcement layout but were subjected to different loading protocols. TUE was subjected to loading along the principal axes (NS and EW) while TUF was subjected to loading in the diagonal directions. Rotation of the collar at the top of the wall was restrained by applying equal displacements with the NS-W and NS-E actuators, which was also practiced by Constantin and Beyer [18]. Note that the loading protocol of TUF also contained small cycles in which a twist was applied at the collar in order to investigate the degradation of the torsional stiffness (see Section 2.4.2). Providing a twist to the wall at diagonal loading positions produced novel results that will complement the data and results from the previous wall tests [8,32]. As previously stated in Section 2.1, neither wall was subjected to an axial load.

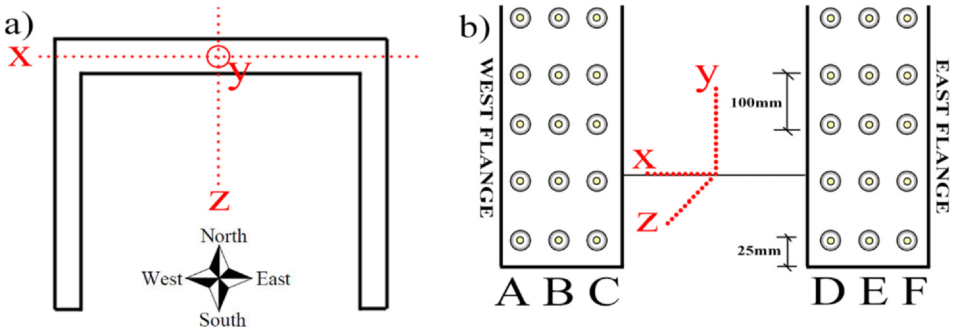


**Fig. 3.** (a) origin and coordinate system of the LEDs (b) LED columns A to E.

One of the primary objectives of this experimental study is to observe if out-of-plane instability can be an issue for slender RC U-shaped walls that have a single-layer of vertical reinforcement. The summary of previous experimental tests on RC walls prone to instability and buckling in Rosso et al. [49] found that all specimens had the common feature of the maximum out-of-plane deformations occurring when the walls were centred (i.e., at 0% drift). Thus, as out-of-plane instability is one of the key focuses of this experimental study on RC U-shaped walls, the loading protocol was adjusted such that out-of-plane instability-prone areas of the wall were not subjected to large compression strains (on reversal of large tension strains). Furthermore, a crushing-type failure mode due to compression of non-planar RC walls has been well documented from previous experimental research, as summarized in Constantin and Beyer [17]. As such, the loading directions that caused wall specimens TUE and TUF to have a large compression zone were limited for this study. For example, the drift level was limited for the wall bending about its minor axis such that the web is in tension, which can lead to a large compression depth in the flanges. Likewise, for specimen TUF, the diagonal loading causing the flange to lead to a large compression zone was limited. The loading positions for both TUE and TUF are shown in Fig. 4b. While the chosen loading protocol here restricts the displacement in some directions past a certain limit, the data obtained up to this limit, as well as the data captured from displacements imposed on the wall in the other directions, will provide invaluable information to help improve the current state of knowledge. The data and information collected from these tests, which is made publicly available (see Section 6, Numerical Data and Reproducibility), will also be beneficial for calibration of finite element models of unconfined RC U-shaped walls with a single layer of vertical reinforcement.

A finite element modelling program VecTor3 [23]was used to obtain a preliminary simulation of the units' behavior. The software and inherent material models have been shown to successfully produce accurate estimates of the force–displacement response of RC U-shaped walls, as well as to give reasonable estimates of the strain distributions up the wall height, in comparison to previous experimental tests [30,31]. A model of the TUE and TUF specimens in VecTor3 estimated that at a drift of 0.4% for position C, the compressions strains at the flange ends of the U-shaped wall (Fig. 4a) would reach 0.2%. Thus, if an ultimate unconfined compression strain of 0.3% is to be assumed [28], limiting the wall about the minor axis with the web in tension (at position C) to a drift ($\delta$) of 0.4% is warranted to prevent a crushing-type failure of the wall. This limiting drift value of 0.4% was also used for the diagonal directional that would cause a large compression zone in the flanges (i.e., positions E and H in Fig. 4b).

### 2.4.1. TUE loading

TUE was subjected to displacements along the principal axes. The loading history for TUE is described below and shown in Fig. 5:

- 0.0% − 0.4% drift: position O-D-C-O-B-A-O, one cycle (increments of 0.1% drift)
- 0.5% − 1.2% drift: position O-D-C*-O-B-A-O, two cycles (increments of 0.1% drift)
- 1.2% − 2.0% drift: position O-D-C*-O-B-A-O, two cycles (increments of 0.2% drift)

* Position C is limited to 0.4% drift

Up to a drift of 0.4%, one-cycle was applied for each drift increment; from 0.5% drift onwards two complete reverse cycles were applied for each in-plane direction at each drift level. The test was stopped once a significant reduction of strength, corresponding to approximately 50% of the maximum strength reached during testing, was observed.

### 2.4.2. TUF loading

The loading history for TUF subjected the U-shaped wall to diagonal displacements. The drift levels indicated are the square root of the sum of squares (SRSS) of the north–south and east–west drifts, discussed further in Section 3.1.3. Furthermore, a small twist was applied at different positions to determine the torsional stiffness of the wall at different drift levels. The loading history is illustrated in Fig. 6 and described below:

- 0.0% − 0.4% SRSS drift: position O-G-H-O-F-E-O, one cycle (increments of 0.2% drift)
- 0.4% − 1.0% SRSS drift: position O-G-H*-O-F-E*-O, one cycle (increments of 0.2% drift)
- 1.0% − 3.5% SRSS drift: position O-D-C[a]-O-B-A-O, two cycles (increments of 0.5% drift)
- 0.0% SRSS drift: position O, apply a twist to determine the elastic torsional stiffness (applied torque of 39 kNm)
- 0.4% and 1.0% SRSS drift: position O, G and H, apply a twist (applied torque of 39 kNm)
- 1.5 and 2.0% SRSS drift: position O, G and H, apply a twist (applied torque of 26 kNm)
- 2.5% SRSS drift: position O and G, apply a twist (applied torque of 13 kNm)

* Position E and H are limited to 0.4% SRSS drift

It should be noted that for specimen TUF one-cycle was performed for each drift increment up to 0.8%, where from 1.0% drift onwards two complete reverse cycles were applied for each in-plane direction at each

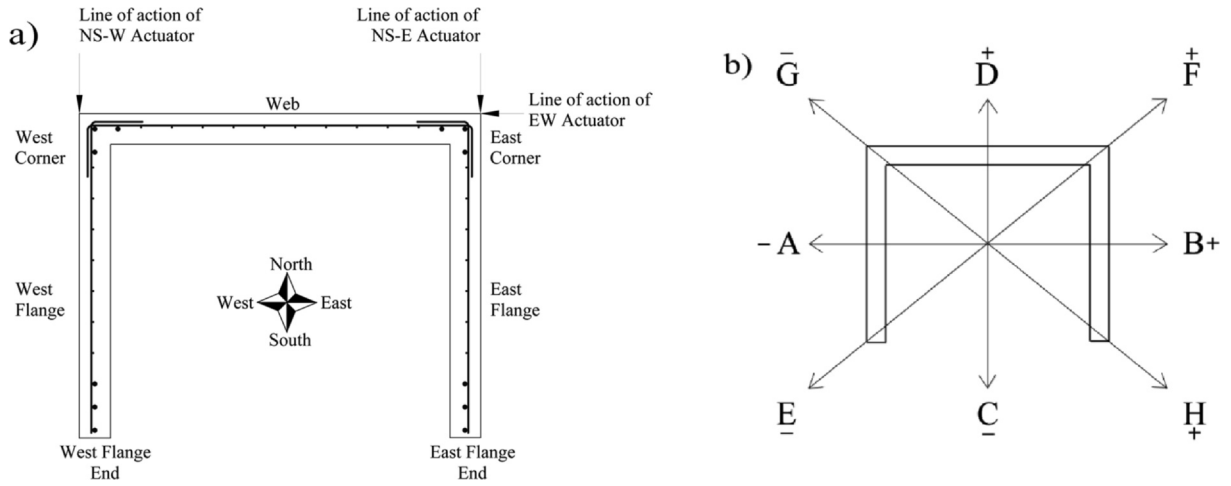


**Fig. 4.** (a) cardinal points, sign convention for forces and displacements, wall parts and (b) loading positions.

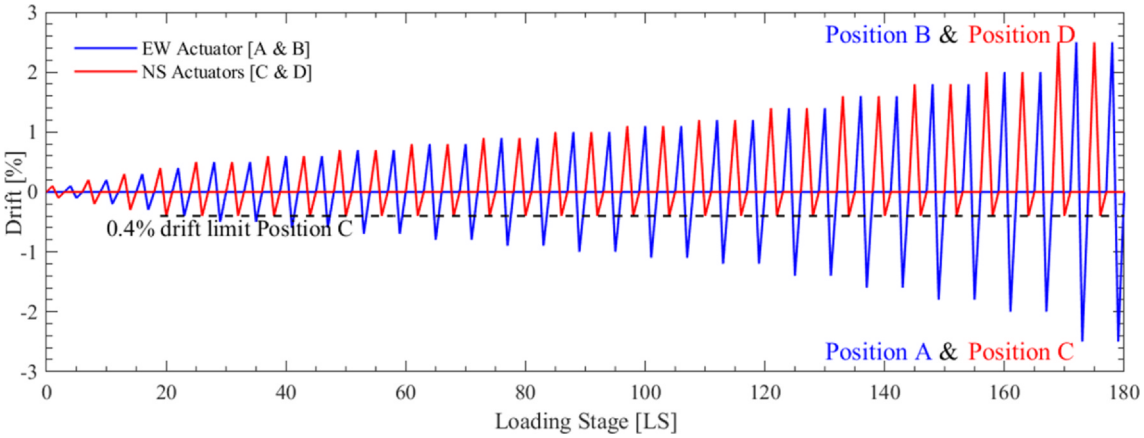


**Fig. 5.** Loading history for specimen TUE.

drift level. As with specimen TUE, the test was considered complete once a significant reduction of strength was observed. Furthermore, twisting of the wall, which was conducted to determine its torsional stiffness, was omitted after 2.5% SRSS drift had been reached at position G, as the stiffness of the wall was significantly degraded after this position and level of drift.

## 3. Test results

The most important findings from the tests are discussed and presented in this section. The failure mechanisms, together with the hysteretic behavior, are discussed in Section 3.1. Yield and ductility estimates are summarized for both walls in Section 3.2 using a simplified, bilinear relationship of the force–displacement response. The influence of the different loading protocols used for each specimen on the cracking patterns are given in Section 3.3. The displacement profile of the boundary ends of the flanges for both specimens, derived from the LED data, is shown in Section 3.4.

### 3.1. Failure mechanisms and hysteretic behavior

#### 3.1.1. Out-of-plane instability failure

In order to inform the discussion of the experimental results, the authors will briefly summarize the development of out-of-plane instability as described by Paulay and Priestley [44]. The illustrations in Fig. 7 apply this explanation to the context of a RC U-shaped wall. At large displacement demands, such as the caused by a moderate-to-large earthquake event, tensile strains greater than yield will develop in the extreme tension fibre region of the wall (Fig. 7a). During the "unloading" stages of the wall, corresponding to a change in direction of the cyclic displacements of the wall, the tensile stresses in the longitudinal reinforcing bars that cross the open cracks will return to zero, the crack widths remain large. Thus, until these cracks close, 'the internal compression force within the wall section must be resisted solely by the vertical reinforcement' [44], as illustrated in Fig. 7b. Due to the out-of-plane inertial response of the wall, coupled with the unavoidable irregularity in the placement of reinforcement, the position of the resultant compression force may not coincide with the centroid of the vertical reinforcement, resulting in transverse curvature and potentially out-of-plane instability Fig. 7c). In fact, the potential for out-of-plane instability failure of walls is exacerbated for the in-plane bending of non-planar sections, such as the T-shaped walls tested in Thomsen and Wallace [53], T-shaped walls in Rosso et al. [49], and the U-shaped walls tested here.

Indications of the out-of-plane instability mechanism were observed throughout the experimental campaign in walls TUE and TUF, along with other failure mechanisms. Detailed descriptions of the failure progression for wall TUE is given in section 3.1.2, and for wall TUF in section 3.1.3.

#### 3.1.2. TUE observations

The failure mechanisms of the specimen TUE are illustrated in Fig. 8 and Fig. 9, while the force–displacement hystereses are shown in Fig. 10. As TUE was loaded along its principal axes, the EW actuator force is plotted against the EW displacement at $h_{EW}$ = 4.65 m (i.e., at the same height as the EW force was applied); for the NS direction, the total force from the NS actuators (NS-E and NS-W, Fig. 4) and the mean top wall NS displacement are plotted in Fig. 10, which have been

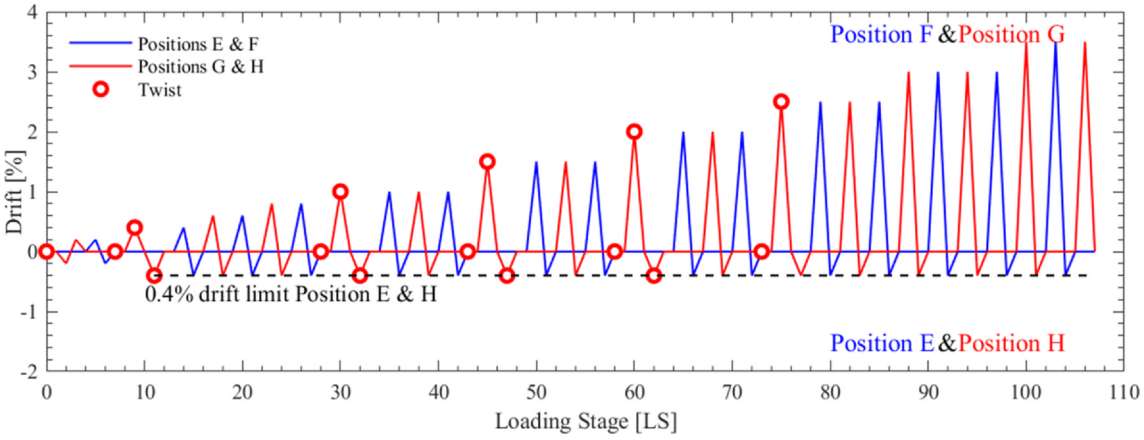


**Fig. 6.** Loading history for specimen TUF.

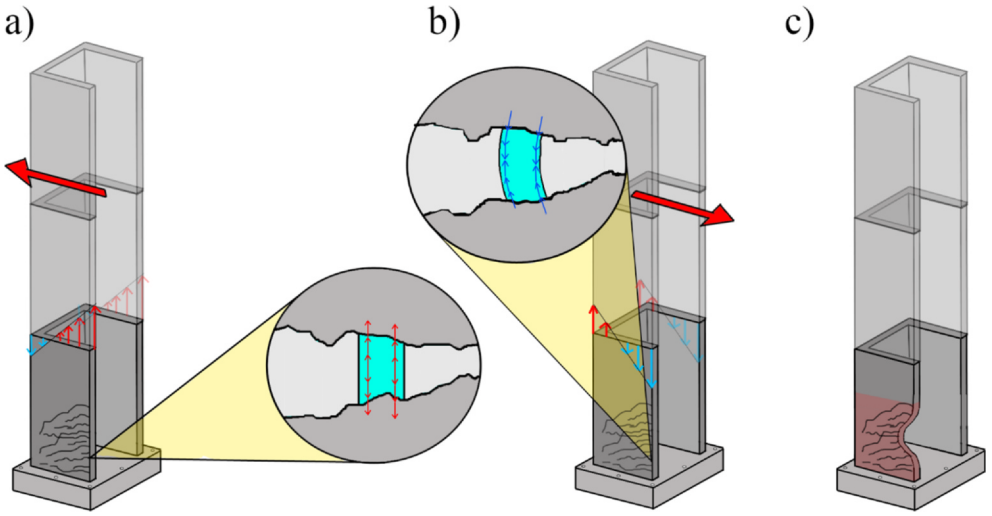


**Fig. 7.** Development of out-plane instability in the flanges ends of a RC U-shaped wall with bending about the principal minor axes (parallel with the flanges) (a) pushing towards D, large tensile strains in lumped reinforcement within boundary ends of the flange, (b) compression forces resisted by reinforcement at open cracks pushing towards position C, (c) out-of-plane instability and buckling occurs.

measured from the LVDTs 2 and 3 recording the NS displacements at $h_{NS}$ = 4.25 m (Fig. 2b).

*3.1.2.1. Local out-of-plane buckling failure mode.* The onset of failure of specimen TUE occurred after splitting cracks formed in the East flange end. Following this, the reinforcing bars in the flange end and one of the two concrete vertical layers buckled out-of-plane. This local failure occurred during loading in the A-B direction (loading parallel to the web) when the East flange was in compression at position B (Fig. 8a). The local out-of-plane buckling occurred during the first stage of the second cycle with a drift of 2.0%. Prior to this failure, the wall had reached 2.0% drift in the direction of position D. When loading to Position C, it is recalled that drifts were limited to 0.4% to avoid a premature compression failure due to the unconfined boundary ends. Because crushing failure at position C was actively prevented by limiting the drift demand to 0.4%, the West and East flange ends were subjected to the largest compressive strains at position A and B, respectively. As a result, local failure occurred at position B due to out-of-plane buckling of the East flange. At position D, a small compression depth exists over the length of the web, which results in a large tension zone in the flanges, causing large tensile inelastic strains at the flange ends. A good distribution of cracking up the wall height of the East and West flange, particularly when pushing towards position D, was observed throughout testing. This is primarily due to the lumped reinforcement in the boundary ends and the small thickness of the walls resulting in a high reinforcement ratio and allowing secondary cracking to occur [29,30,36]. Larger crack widths could be observed for the first 3–4 primary cracks up from the wall base when the wall was pushed to position D. More details on the crack distribution of the walls is given in Section 3.3.

The development of out-of-plane deformation in the flanges was more or less consistent with the explanation of the behavior given in Section 3.1.1, taking place during compressive loading cycles following large tensile strains in the longitudinal rebar. The type of buckling observed in TUE, and also in TUF as described in Section 3.1.3, is consistent with the definition given in Dashti et al. [21] of a local failure, rather than a global out-of-plane failure due to in-plane loading, where: (i) there were generally greater, and wider, cracks at the base region, indicating localization of tensile strains that exhibit bar buckling, (ii) a gradual strength degradation was observed, rather than sudden drop in strength, and (iii) the out-of-plane deformation was limited to a height from the base of the boundary region of the flange.

The rebar buckling in specimen TUE is comparable to the mode of failure observed in specimen P10 from Menegon et al. [39], as shown in Fig. 8c. Several boundary element prisms, representative of end regions of non-ductile RC walls, were tested by Menegon et al. [39] under cyclic

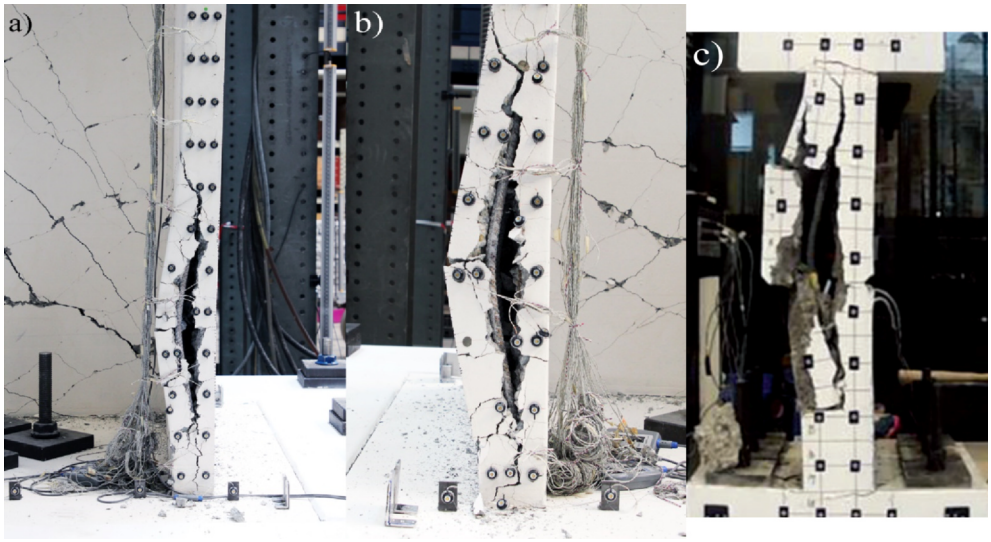


**Fig. 8.** Local out-of-plane buckling observed in specimen TUE in (a) boundary ends of the East flange during loading to position B at 2.0% drift (b) boundary ends of the West flange during loading to position C after reaching 2.5% drift at position D and (c) failure mode of specimen P10 reported in Menegon et al. [39]


**Fig. 9.** Specimen TUE (a) cracking distribution shown at the back of the web [position B, 2.0% drift] (b) close-up on the large, open crack at the back of the web leading down to the East flange-web intersection [position B, 2.0% drift] (c) condition of the web at the end of testing.

uniaxial tension–compression, with specimen P10 having a thickness of 130 mm and detailed with a central layer of three vertical reinforcing bars of 16 mm diameter, characteristics that are strikingly similar to the boundary ends of the flanges of TUE (and TUF). The authors note that the bar buckling in P10 initiated at a lower tension strain due to the vertical splitting of the specimen, which indicated 'that local bar buckling is potentially worse in singularly reinforced walls' [39] in comparison to walls with two layers of vertical reinforcement primarily because of the absence of stirrups or crossties in singularly reinforced walls. The rebar buckling in TUE can also be compared to specimen TUC, tested by Constantin and Beyer [18]. In wall TUE, the buckling of the boundary end only occurred in the plastic zone, which was similarly observed for the flange with lumped reinforcement in TUC. Specimen TUC was detailed such that one flange had lumped longitudinal reinforcement at the boundary end and the other had distributed longitudinal reinforcement; failure of TUC occurred due to out-of-plane instability initiating in the flange end that contained lumped reinforcement followed by crushing of the concrete, as in TUE. The flange in TUC with distributed reinforcing showed no instability issues during the test.

As no significant reduction in strength had been observed with the rebar buckling in the East flange, the test was continued, and a similar rebar buckling at the West flange end was observed when pushing towards C after having reached for the first time 2.5% drift for position D (Fig. 8b); the drift towards C remained limited to 0.4%. At position D at 2.5% drift the lumped longitudinal bars in the boundary of the West flange were subjected to large tensile strains at the distributed and large cracks in the plastic region of the wall. This resulted in the out-of-plane buckling observed when returning to Position O and pushing the wall to the limiting drift at position C.

The local out-of-plane buckling in the West flange corresponded to a drop in the shear force by almost 45% when comparing the force attained at position C in the previous cycle. As the drifts were limited to 0.4% in the direction of position C, when the exposed rebar would be most vulnerable, the testing continued, as wall specimen TUE showed no strength degradation in the EW direction (i.e., positions A and B).

*3.1.2.2. Compression failure mode.* As noted in the previous section, while a drop-in strength of approximately 44% was observed after the localized out-of-plane buckling failures occurred, limiting the displacement towards position C meant that the test could continue without concern as large compression strains could not be induced in the boundary regions of the flanges. Even for when the wall was subjected to large drifts in the East-West direction (position A and B), large compression strains were more likely to be expected in the corners of the intersecting regions of the flange and web, rather than the boundary ends of the flange, primarily due to the phenomenon known as shear lag [31].

A large compression strut in the web leading down to the corners of the wall was observed throughout the test, where a large crack in the web (≈5-7 mm) was present once the boundary end of the East flange had buckled (Fig. 9a and b). As testing continued after observing the localized out-of-plane buckling failures, the concrete crushed in the corners of the web-flange regions during the second cycles of 2.5% drift to positions A, B and D, resulting in shear-sliding along a primary crack in the web and ultimately the loss of concrete within this region of the wall. Correspondingly, a drastic drop in shear strength (≈72%) was observed, instant at which the testing of TUE was stopped.

### 3.1.3. TUF observations

The failure mechanisms of specimen TUF are shown in Fig. 11 and Fig. 12, while the force–displacement hystereses are shown in Fig. 13.

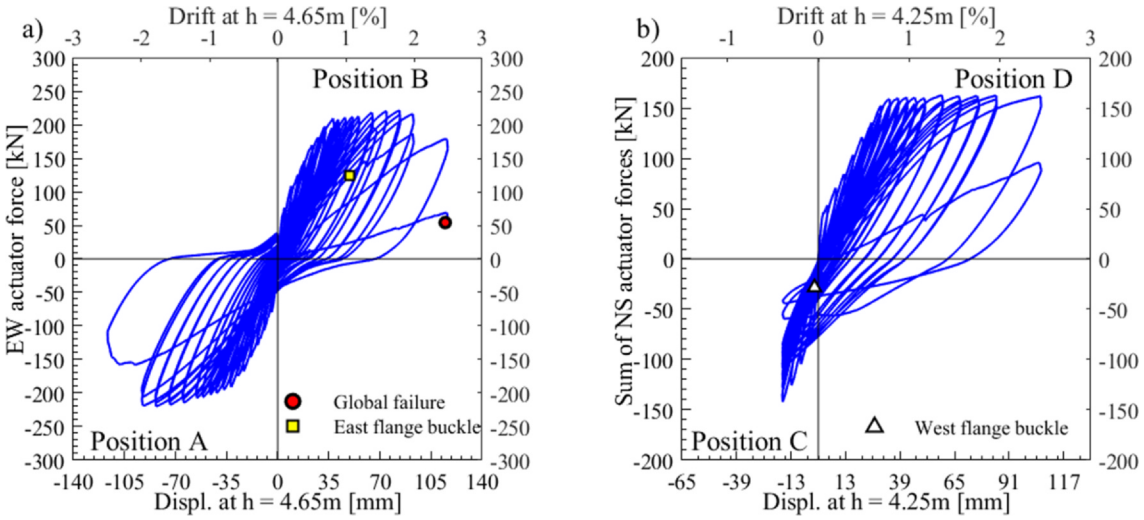


**Fig. 10.** Specimen TUE: force–displacement hystereses for (a) east–west direction (position A and B) and (b) north–south direction (position C and D).

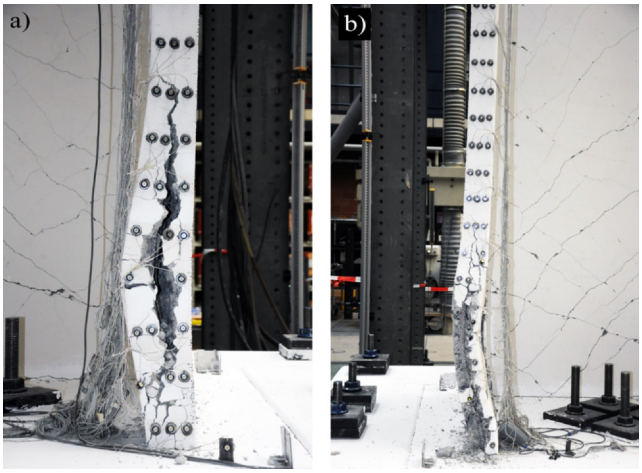


**Fig. 11.** Out-of-plane buckling observed in specimen TUF in (a) the East flange during loading to position H after reaching SRSS 2.5% drift at position G and (b) West flange during loading to position E after reaching SRSS 2.5% drift at position F.

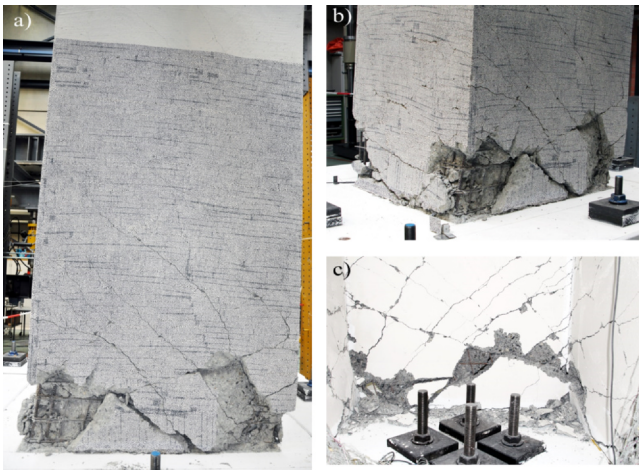


**Fig. 12.** Specimen TUF: Global wall failure due to concrete crushing in the web (a and b) sliding along shear cracks in web at [3.5% SRSS drift, position G] (c) crushing at the toe of the wall where the back of the web intersects the West flange [at the end of test]

As a diagonal loading protocol was used for TUF, the individual actuator forces, as well as their resultant, are plotted against the top wall displacements, which were measured by LVDTs recording the horizontal NS and EW displacements at $h_{NS}$ = 4.65 m and $h_{EW}$ = 4.25 m (Fig. 4). Importantly, the top wall displacements and forces were used to calculate the square root of the sum of squares (SRSS) (Equations (1) and (2)) in order to obtain representative quantities for the diagonal direction (Fig. 13b-c), which was similarly used by Constantin and Beyer [18].

$$\boldsymbol{F_{SRSS}} = \sqrt{\boldsymbol{F_{EW}^2} + \boldsymbol{F_{NS}^2}} \,.\, \boldsymbol{sign}(\Delta_{NS}) \tag{1}$$

$$\Delta_{SRSS} = \sqrt{\Delta_{NS}^2 + \Delta_{EW}^2} \,.\, sign(\Delta_{NS}) \tag{2}$$

where $F_{EW}$ and $F_{NS}$ are the forces carried by the wall in the EW and NS directions respectively ($F_{NS}$ is the sum of the forces in the two actuators in this direction), while $\Delta_{EW}$ and $\Delta_{NS}$ are the in-plane horizontal displacements in the EW and NS directions respectively. Note that the SRSS values are multiplied by the sign (positive or negative) of the $\Delta_{NS}$ for plotting purposes. Furthermore, $\Delta_{NS}$ is calculated as the average between the displacements recorded by the LVDTs 2 and 3 at the North-South East ($\Delta_{NS\text{-}E}$) and North-South West ($\Delta_{NS\text{-}W}$) ends of the wall (Fig. 2b).

*3.1.3.1. Local out-of-plane buckling failure mode.* Specimen TUF experienced local out-of-plane buckling of the East flange during loading in the G-H direction for the first cycle of 2.5% SRSS drift. The out-of-plane buckling occurred after extensive horizontal cracks opened up in the boundary ends of the East flange when the wall was pushed to position G; on returning to position O, the plastic zone of the East flange noticeably buckled inwards before the boundary end split open (Fig. 11a), revealing the lumped longitudinal reinforcement, at approximately zero displacement (i.e. when the wall was centered). The bars buckled inwards, towards the center of the wall, as the wall was continued to be pushed towards the limiting displacement at position H. This type of failure mode corresponds to the same failure mode seen in specimen TUE, which also occurred at a similar displacement demand. TUF reached approximately 83 mm and 67 mm for $\Delta_{EW}$ and $\Delta_{NS}$, respectively, at Position G just prior to buckling, corresponding to a drift of 1.9% and 1.6% drift respectively; for TUE, the local out-of-plane buckling occurred during the starting stage of the second cycle with a drift of 2.0%. As no significant reduction in strength had been observed, the test continued, and a similar local out-of-plane buckling of the boundary end of the West flange was observed during the load cycle towards position E (Fig. 11b), after having reached 2.5% SRSS drift at position F. In this last case, the rebars buckled outwards (i.e., towards the exterior of the unit).

No significant drop in force was observed by either of the two local out-of-plane buckling failures, primarily due to the limiting drifts at position E and F, thus the testing of specimen TUF continued. As discussed in the previous section and as should be emphasized here again, without limiting the drifts in the direction causing large compression strains in the flange ends, it is likely that global failure would have occurred during these drift cycles, corresponding to crushing of the flange ends rather than the local (or global) instability. For example, specimen TUC from Constantin and Beyer [18] also experienced an out-of-plane buckling failure after reaching 2.5% SRSS drift. However, the wall stiffness of specimen TUC was significantly reduced when the wall was loaded from position O towards position E, where the test was stopped at 1.0% SRSS drift due to extensive damage; for the testing that was presented here for specimen TUF, the SRSS drifts were limited to only 0.4% SRSS in this direction of loading for primarily this reason. Also, it should be noted that the boundary ends and corners of specimen TUC from Constantin and Beyer [18] were heavily confined, thus a greater compression strain capacity would have been possible in the boundary ends of the flanges of TUC in comparison to the unconfined specimens TUE and TUF tested here. It has also been shown that buckling prone reinforcing bars fail much earlier in comparison to reinforcing bars with limited or no buckling due to the detrimental effect of low-cycle fatigue [54], which make these types of walls particularly susceptible.

A video showing the local out-of-plane buckling failures of the boundary ends of specimen TUF can be found in the electronic version of this journal paper (i.e., see Video 1 online). It is evident from this video that bar buckling occurred before the concrete had crushed. In the video, it appears that, after the steel bars in the yielding region lost bond with the concrete and elongated in tension, on reversal the bars were constrained in compression by the surrounding decoupled concrete. If the plasticity in the steel is large enough, on this reversal, the steel bar forces its way out of the concrete wall, shown in the attached video as a vertical split at the boundary end that opens up as the bar buckles outwards.

*3.1.3.2. Final compression failure mode in the web.* Global failure of Specimen TUF ultimately occurred due to compression failure of the wall at the web-flange intersection while pushing the wall to position G at 3.5% SRSS drift (Fig. 12). Failure at this position initiated as the displacement $\Delta_{EW}$ displacement reached 115 mm, corresponding to a

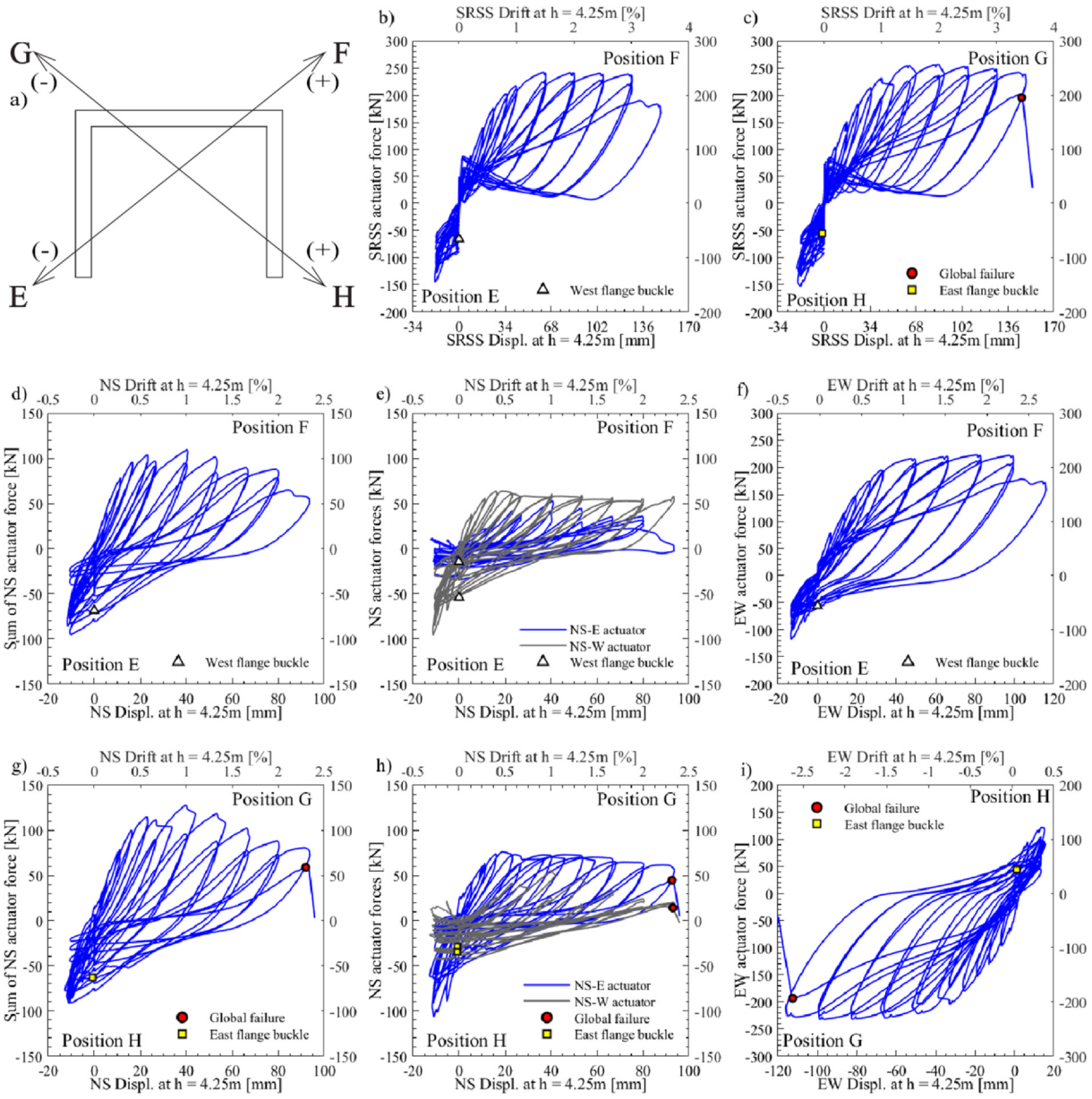


**Fig. 13.** Specimen TUF: (a) loading positions (b and c) SRSS force–displacement hystereses and (d – i) for the individual NS and EW directions.

SRSS drift of 3.5% SRSS, where shear sliding could be observed in the web once a large crack opened at the bottom of the web (Fig. 12a). The shear sliding immediately caused the corner of the intersecting region of the web and West flange to crush, which produced a noticeable separation between two sections at the base (Fig. 12c). Due to the shear-sliding, a small reduction of strength was observed, where the SRSS forces dropped from 202 kN to approximately 180 kN. However, the crushing and separation of the web and West flange caused a much larger reduction of strength, corresponding to SRSS forces to drop from 180 kN to just 28 kN, a reduction of 84%. The large decrease in strength meant that testing was stopped for specimen TUF.

### 3.2. Bilinear force–displacement response

Simplifying the force–displacement relationship of the walls from Fig. 10a,b and Fig. 13b,c to a bilinear response [35]), the approximate first yield displacement and force ($\Delta_y'$ and $F_y'$), nominal yield displacement, and ultimate displacement and force ($\Delta_u$ and $F_u$ respectively) were determined for position A, B, D, F, and G and are given in Table 4. The bilinear relationship was found assuming that $\Delta_y'$ corresponds to the displacement at $0.75F_u$, where extrapolating a straight line from the origin through the point at $\Delta_y'$ to meet $F_u$ corresponds to the nominal yield ($\Delta_y$; the nominal yield also corresponds to a ductility ($\mu$) of 1. The drifts corresponding to first yield, nominal yield and ultimate displacements are also given in Table 4 ($\delta'_y$, $\delta_y$ and $\delta_u$ respectively). The $\mu$ values in Table 4 for specimen TUF (at positions F and G) with diagonal loading are greater than the $\mu$ values for TUE (at positions A, B, and C) with loading applied along the principal axes. However, if the EW and NS displacement components of the loading are compared at the ultimate state of the walls, similar values of the ultimate displacement ($\Delta_u$) are observed. For example, the $\Delta_u$ 148.7 mm at position F in Table 4 is the result of the SRSS of $\Delta_{EW}$ (position B) 115.6 mm and $\Delta_{NS}$ (position D) 93.5 mm, which are comparable to the $\Delta_u$ of specimen TUE for those directions of loading. It is emphasized here that the ductility values for TUE and TUF (in Table 4) should be interpreted with some caution, as these walls were subjected to limited drifts in the directions that would typically produce large compression strains at the ends of the flanges; if loading had not been limited in these directions, it is likely that a non-

**Table 4**
Bilinear force–displacement response values for specimen TUF.

| Position | $\Delta_y^{'}$(mm) | $\delta_y^{'}$(%) | $\Delta_y$(mm) | $\delta_y$(%) | $\Delta_u$(mm) | $\delta_u$(%) | $\mu$ | $F_y^{'}$(kN) | $F_u$(kN) |
|---|---|---|---|---|---|---|---|---|---|
| A-B | 22.8 | 0.49 | 30.4 | 0.65 | 116.4 | 2.50 | 3.8 | 166.2 | 221.6 |
| D | 21.1 | 0.49 | 28.1 | 0.66 | 106.5 | 2.50 | 3.8 | 122.4 | 163.2 |
| F | 28.2 | 0.66 | 37.6 | 0.88 | 148.7 | 3.45 | 3.9 | 182.0 | 242.6 |
| G | 29.8 | 0.70 | 37.5 | 0.88 | 153.8 | 3.62 | 4.1 | 192.9 | 242.6 |

ductile, crushing-type failure would have been observed for both wall specimens and at lower ductility capacities than those indicated in Table 4. The ductile reinforcing bars used in the boundary ends (previously discussed in Section 2.2) also allowed the walls tested here to achieve high ductilities, whereas low-ductility welded wire mesh has been used in Colombian construction practice [13,12]. Thus, a wall detailed with low-ductility steel could result in a brittle failure due to fracturing of the bars, which can also be exacerbated with the phenomenon of low-cycle fatigue [54].

### 3.3. Crack patterns

Previous discussions on crack patterns for RC U-shaped walls have found that the loading directions of positions E and H resulted in the steepest cracks in the flanges and web, which opened in the upper half of the wall [8,18]. However, these directions of loading were either not part of the protocol used for TUE or were limited for TUF. Thus, the critical cracking distributions observed for the testing presented herein is quite different to that reported previously.

The steepest cracks observed during testing for both walls were present in the web, rather than the flanges. For TUE, the steepest cracks in the web occurred while pushing the wall to positions B and A (Fig. 14a and Fig. 14b, respectively), while for TUF, the steepest cracks in the web occurred while pushing the wall to positions F and G (Fig. 15a and Fig. 15b, respectively). It should also be noted that specimens TUE and TUF tested as part of this research project had a larger shear span ratio (Table 1, also known as the flexure-to-shear strength ratio), owing to the larger height of the walls in comparison to the previous tests on RC U-shaped walls [8,18], which also contributed to the cracking distribution differences discussed here. The cracking patterns were obtained from the DIC images captured during testing (Section 2.3.3) and processed using the 3D-digital image correlation tool VIC 3D (Correlated [19] to calculate the major principal strains, which reveals the cracking patterns given in Fig. 14 and Fig. 15. Note that Fig. 15a and Fig. 15b show the cracking pattern at SRSS 2.5% drift, which correspond to an in-plane EW drift of approximately 2.0%, comparable to the in-plane drift subjected to wall specimen TUE and corresponding crack patterns shown in Fig. 14a and Fig. 14b. Interestingly, the cracks appear to be more open and steeper for in-plane loading to positions A and B (specimen TUE) than to the diagonal loadings of positions F and G (specimen TUF) at comparable drift levels. Nevertheless, these crack patterns in the web indicate the increased shear demand that was imposed on the wall, in comparison to what would be expected for a rectangular wall, for these different loading positions. For example, the crack patterns observed in the U-shaped wall tested here can be compared to the rectangular specimens tested in Dazio et al. [22], which had similar shear span ratios (given in Table 1) of approximately 4.5 m. While the crack patterns in the rectangular wall specimens from Dazio et al. [22] appear to have some steep cracks, the walls are dominated by the horizontal-flexural cracks at the base. These crack pattern observations also corroborate the difference in shear deformation demands for rectangular and nonrectangular walls discussed in Beyer et al. [9].

The crack patterns in the flanges were starkly different to that observed in the web for both specimens during loading. The large shear span ratio resulted in the walls being governed by flexural actions, rather than shear, for loading applied parallel to the flanges; the crack patterns appear to be more horizontal along the flanges (Fig. 14c,d) than along the web (Fig. 14a,b), likely to be related to the larger shear span ratio for loading in the direction of the flanges (see Table 1). Furthermore, as previously acknowledged in Section 3.1.2.1, the large longitudinal reinforcement ratio, primarily due to lumped vertical

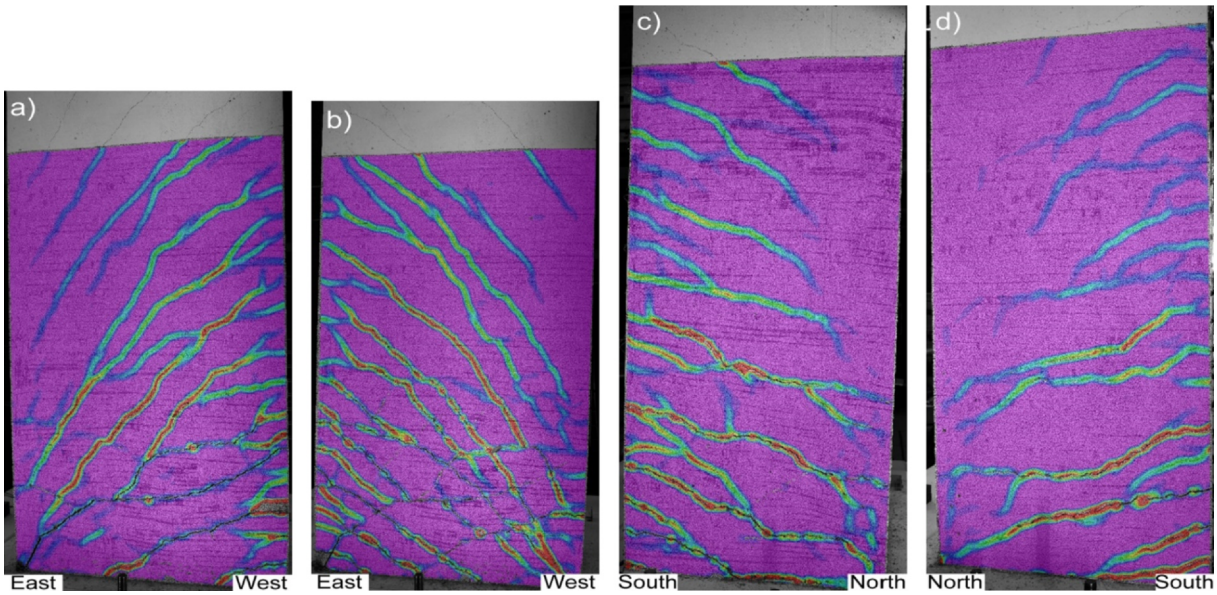


**Fig. 14.** Crack patterns for specimen TUE at the end of 2.0% drift cycle: (a) Web, position B (b) Web, position A (c) East flange, position D and (d) West flange, position D.

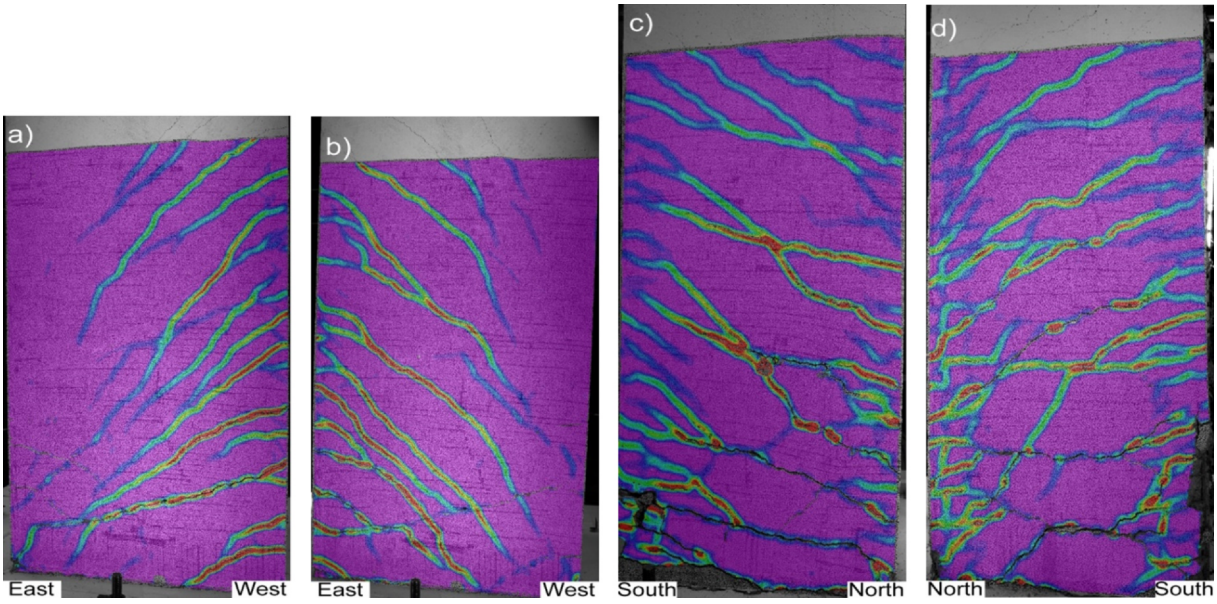


**Fig. 15.** Crack patterns for specimen TUF: (a) Web, position F, SRSS drift 2.5% (b) Web, position G, SRSS drift 2.5% (c) East flange, position G, SRSS drift 3.0% and (d) West flange, position F, SRSS drift 3.0%

reinforcement in the boundary ends, meant that secondary cracking would occur as the wall was pushed parallel with the flanges and towards the web, resulting in a good distribution of cracks up the wall height. As previously mentioned in Section 3.1.2.1, for this direction of loading, the large web area, due to the presence of the flange, results in a small compression depth and good flexural performance. This type of behavior is exemplified in Fig. 14c and Fig. 14d for specimen TUE, which shows flexural cracks governing the walls performance for the East and West flange, respectively, at position D with a drift of 2.0%. Furthermore, similar cracking distributions in the East and West flanges can be observed in Fig. 15c and Fig. 15d for specimen TUF while pushing the wall to position G and position F, respectively, for a SRSS drift of 3.0%. The flexural cracks in the flanges of TUF higher up on the wall appear to run the entire length of the flange in comparison to TUE, which only cover approximately 75% to 50% of the flange length. The extra lengths covered by the cracks in the flanges of TUF are due to the diagonal loading that is subjected to the wall, where the additional displacement in the EW results in the flanges being subjected purely to tension at these diagonal positions, rather than the in-plane loading of TUE, which would create a strain profile over the length of the flange.

### 3.4. Displacement profile and out-of-plane behavior

Using the data obtained from the LEDs (Section 2.3.2) attached to the surface of the boundary ends of the flanges, which extend up the height of the wall, it is possible to obtain the displacement profile at critical loading stages. This section provides displacement profile observations of the boundary ends of the wall for specimen TUE (Section 3.4.1) and TUF (Section 3.4.2).

#### 3.4.1. TUE displacement profile

Fig. 16 presents the out-of-plane displacement profile of the boundary ends of specimen TUE as a function of drift at position O (i.e., when the wall is centered). It should be noted that “out-of-plane” here is defined by displacements of the LEDs in the x-direction (Section 2.3.2, Fig. 3) relative to their starting position at position O for each drift cycle. Furthermore, the displacement profiles given in Fig. 16 are the average of the out-of-plane displacement for each row of LEDs up the wall height. Importantly, the drift indicated in the legends of Fig. 16 is that reached by the wall at position D (second cycle), whereas the profiles are calculated at position O. For the lower 1000 mm of the boundary end of the East Flange (Fig. 16b), the out-of-plane displacements progressively increase as a function of the imposed drift, until failure. In contrast, the boundary end of the West flange in Fig. 16a only demonstrates a noticeable out-of-plane deformation in the last few drift cycles, where the largest deformations prior to failure were concentrated in the lower 500 mm.

Using the LED data, the in-plane drift towards positions C and D ($\delta_{CD}$) is plotted in Fig. 17 as a function of the maximum out-of-plane deformation ($\Delta_{oop}$) of the boundary ends of the West and East flange. It should be noted that the $\Delta_{oop}$ here have been normalized to the thickness of the wall ($t_w$ = 100 mm). Furthermore, it was possible to plot $\delta_{CD}$ as a function of $\Delta_{oop}$ because these two measurements of displacement were perpendicular to one another. The authors do not provide $\Delta_{oop}$ as a function of drift towards positions A and B, where the direction of out-of-plane deformations aligns with the imposed displacement. The $\Delta_{oop}$ of the East flange (Fig. 17b), which was observed to inelastically buckle before the West flange, is found to increase incrementally with increasing drift $\delta_{CD}$. As discussed in Section 3.1.2.1, inelastic buckling of the East flange was observed to have occurred while pushing the wall to position B, and hence the point of failure cannot be provided in Fig. 17b. Interestingly, the out-of-plane deformations were observed to be sustained by the East flange pushing towards position C (in the negative drift direction of Fig. 17b) prior to the inelastic buckling observed. This contrasts with the experimental findings on slender RC walls from [49], where it was found that the maximum out-of-plane deformations occurred when the walls were centered (i.e., at a drift of 0%) and failed with a global out-of-plane response. The results in Fig. 17b for the East flange further supports the supposition that the U-shaped walls here experienced local out-of-plane buckling failures. However, the West flange (Fig. 17a) appears to only have had some out-of-plane deformation ($\Delta_{oop}$) in the final few cycles prior to the observed out-of-plane buckling failure. Moreover, the largest $\Delta_{oop}$ for the West flange on each cycle appear to occur when the wall was centered (i.e., at position O), where failure also approximately occurred at this position.

An expression by Paulay and Priestley [44] (Equation (3)) was developed to estimate the critical level of out-of-plane deformation ($\zeta_{cr}$) that can be resisted by a wall before inelastic buckling occurs, where $\zeta_{cr}$ in Equation (3) is normalized to the wall thickness.

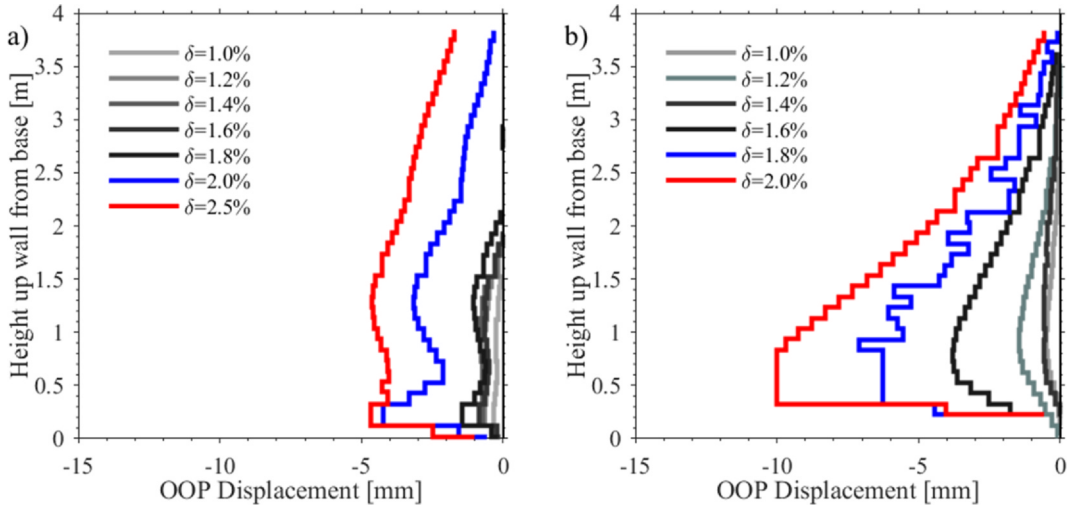


**Fig. 16.** Out-of-plane displacement profiles of TUE at position O for different levels of drift and for (a) the West flange and (b) East.

$$\zeta_{cr} = 0.5(1 + 2.35m - \sqrt{5.53m^2 + 4.70m}) \quad (3)$$

where $m$ is the mechanical reinforcement ratio ($m = \rho_{be}(\frac{f_y}{f_c})$).

Using the wall parameters from Table 1 and material properties from Table 2 and Table 3 for wall specimen TUE, a $\zeta_{cr}$ value of 0.12 is obtained. Superimposed in Fig. 17 is the $\zeta_{cr}$ calculated for specimen TUE using Equation (3). The calculated $\zeta_{cr}$ is consistent with the observed out-of-plane deformation that was sustained by the East and West flanges of TUE before inelastic buckling was observed.

### 3.4.2. TUF displacement profile

Fig. 18 presents the out-of-plane displacement profile of the boundary ends of specimen TUF as a function of SRSS drift at position O (i.e., when the wall is centered after having been pushed to either position G or F, and on its way to positions E or H). It should be noted again that, while specimen TUF was subjected to diagonal loading, "out-of-plane" here is defined by displacements of the LEDs in the x-direction (Section 2.3.2, Fig. 3) relative to their starting positions at O. Importantly, the SRSS drift indicated in the legends of Fig. 18 is that reached by the wall at either position F or position G (first cycle) for the West flange (Fig. 18a) and East flange (Fig. 18b) respectively, whereas the profiles shown are those that are calculated at position O as the wall is pushed towards either position H or position E. The boundary end of the West flange of TUF at position O (Fig. 18a) appears to behave more like the boundary ends of specimen TUE with loading along the principal axes (Section 3.4.1), where the direction of out-of-plane deformation occurs to the west and progressively increases with increasing drift. In contrast, the East Flange (Fig. 18b), the out-of-plane displacements of the lower ≈800 mm appear to progressively increase, particularly for the last two SRSS drift cycles, prior to failure. This length above the base of the wall also corresponds to the length of approximately 840 mm over which out-of-plane buckling was observed to occur in the East flange (Fig. 8a). Interestingly, above this length, the boundary end of the East flange bends towards the East, which is more prominent for the SRSS drift of 2.5% corresponding to the localized failure observed.

## 4. Torsional stiffness of specimen TUF

As discussed in Hoult and Beyer [32], it is likely that a RC U-shaped wall will twist if a building is subjected to earthquake ground motions, which is primarily due to the position of the shear center being outside of the section and any asymmetries of the building plan layout typically leading to an offset between the center of stiffness and center of mass. Thus, given the paucity of research that has focused on the torsional performance of RC walls, the authors found it important to extend the available experimental evidence of the performance of RC U-shaped walls subjected to a twist.

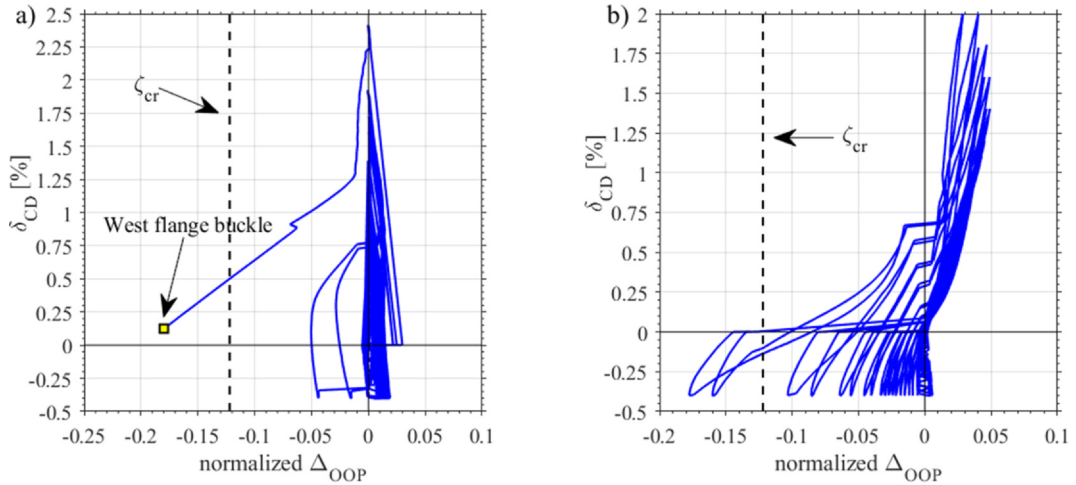


**Fig. 17.** Specimen TUE: in-plane drift in the direction of positions C and D ($\delta_{CD}$) as a function of normalized maximum out-of-plane deformation ($\Delta_{oop}$) of the boundary ends (a) west flange (b) east flange.

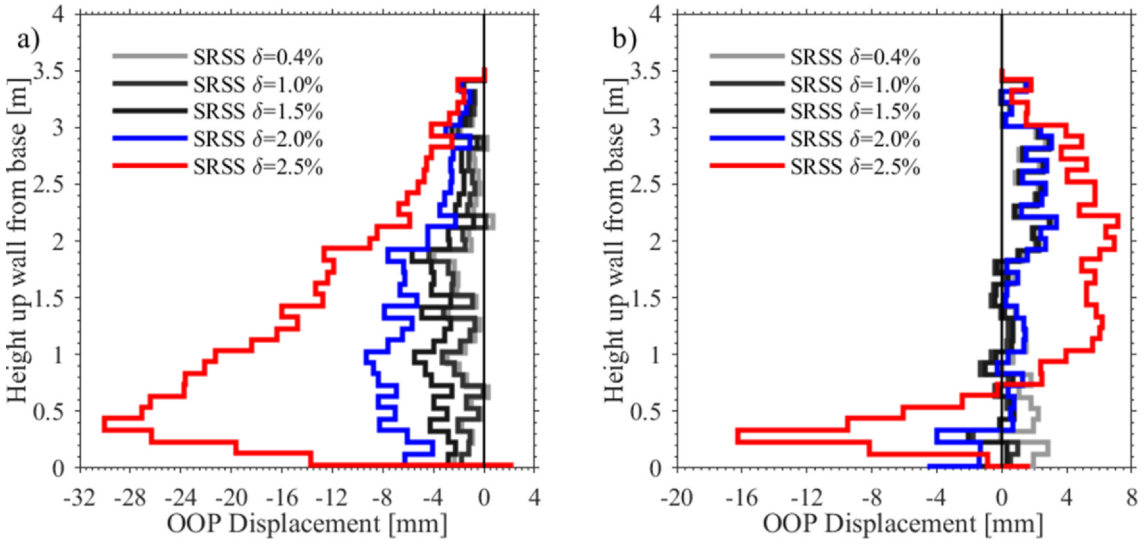


**Fig. 18.** Out-of-plane displacement profiles of TUF at position O for different levels of drift for (a) the West Flange and (b) East flange.

The research conducted in Hoult and Beyer [32] focused on the torsional stiffness of RC U-shaped walls subjected to translational displacements along the principal axes (i.e., positions O, A, B, C and D), which used the experimental dataset from Beyer et al. [10]. The results from Hoult and Beyer [32] showed that the torsional stiffness of a wall that is loaded beyond cracking is considerably smaller than the elastic, uncracked wall and that the torsional stiffness decreased with increasing in-plane translational displacement. The diagonal loading protocol of TUF presented an opportunity to research the torsional stiffness of RC U-shaped walls loaded diagonally, which would give new insights into the torsional performance of such walls.

The torsional moment is given as a function of rotation in Fig. 19 for specimen TUF and at the different positions and drift levels where the wall was subjected to a twist (discussed in Section 2.4.1). It should be noted that as local out-of-plane buckling had been observed in the East Flange at a SRSS drift of 2.5% pushing the wall to position G to H, it was decided not to conduct the twisting of the wall beyond this load step. The rotations (in milliradian) and the torque (in kNm) were calculated using Equation (4) and (5):

$$\theta = \frac{\Delta_{NS-E} - \Delta_{NS-W}}{1.3\boldsymbol{m}} \tag{4}$$

$$T = \frac{F_{NS-E} - F_{NS-W}}{2} \cdot 1.3m \tag{5}$$

where $\Delta_{NS\text{-}E}$ and $\Delta_{NS\text{-}W}$ are the displacements (in mm) in the NS direction recorded at the east and west side of the web and measured at a height of 4.25 m above the foundation (Fig. 1b). The 1.3 m in the denominator of Equation (4) is the distance between the NS actuators and also between the LVDTs measuring the displacements $\Delta_{NS\text{-}E}$ and $\Delta_{NS\text{-}W}$ (in meters). The applied torque was simply calculated as the difference between the actuator forces in the NS direction multiplied by the lever arm (Equation (5)).

There are many observations that can be made from the torsional-rotation curves in Fig. 19. At position O (Fig. 19b), it can be seen that the torsional stiffness decreases as a function of increasing drift (or displacement demand), which conforms with the experimental observations from Hoult and Beyer [32]. The torsional stiffness is defined here as the ratio of torque-to-rotation between the points of maximum rotation; more specifically, the torsional stiffness is defined as the secant stiffness connecting the maximum and minimum torque moment. The torsional stiffness ($J_R$) values are given in Table 5 as a function of ductility ($\mu$). The ductility values are determined using the yield displacement ($\Delta_y$) estimates in Table 4. The tabulated values show that, once the wall is loaded well in its inelastic range ($\mu$ greater than1.5), the torsional stiffness at position O is smaller than at the peak translational displacements. This also conforms with the observations from Hoult and Beyer [32]. This response is attributed to the stiffening effect of compression zones with regards to the twisting actions, which are present at position G and H but not at position O. Although at position H (Fig. 19d) the drift was limited drift to 0.4%, a clear decrease in rotational stiffness can be observed as a function of the drift demands applied to the wall in the other directions preceding position H (as given in the legend of Fig. 19d). Furthermore, at this position the East flange would largely be in compression, resulting in the West flange and web (in tension) being able to move more freely and resulting in the larger rotations that are shown in the third quadrant of Fig. 19d. At position G (Fig. 19c), residual rotations can be observed on return to a force-couple of zero; compare the curves for drifts of 0.4% and 1.0%, for example, with the same applied force-couple of 30 kN. This observation of residual rotations was also reported in Hoult and Beyer [32] for the numerical results of the U-shaped walls with zero axial load at position A; the explanation given was that, as no axial load is applied, the flange in tension is able to rotate more freely in comparison to the flange in compression for the same applied force. Furthermore, in Fig. 19c, the torque-rotation curves at drifts of 1.5% and 2.0% at position G almost superimpose one another, with corresponding $J_R$ values of 5.8 kNm/mrad and 5.7 kNm/mrad respectively. It should be noted that the force-couple to twist the wall decreased as the drift increased (i.e., 30 kN used for drifts of 0.4% and 1.0%, in comparison to 20 kN used for drifts of 1.5% and 2.0%), which explains the larger maximum rotation reached for drifts of 1.0% in comparison to drifts at 2.0%. There is an apparent increase in $J_R$ at position G for 2.5% SRSS drift (Fig. 19c). This is attributed to the reduced torque moment that was applied at 2.5%. Fig. 19c shows that the torque-rotation relationship at 2.5% follows closely the one at 2.0% from a zero rotation up to a rotation of 1‰, i.e., the rotational stiffness at 2.0% and 2.5% seems to be effectively the same.

Some of the observations above are further substantiated in Fig. 20, where the $J_R$ values are normalized to the elastic, uncracked torsional stiffness ($J_{R.el}$, determined experimentally as 18.7 kNm/mrad in Table 5) and plotted as a function of ductility ($\mu$). Superimposed in Fig. 20 are the normalized torsional stiffness values from Hoult and Beyer [32] and the normalized translational stiffness ($K_x$ values; the $K_x$ has been normalized to the elastic translational stiffness of the uncracked wall as determined in Hoult and Beyer [32]. The secant stiffness is computed assuming the wall behaves as an ideal elastoplastic system.

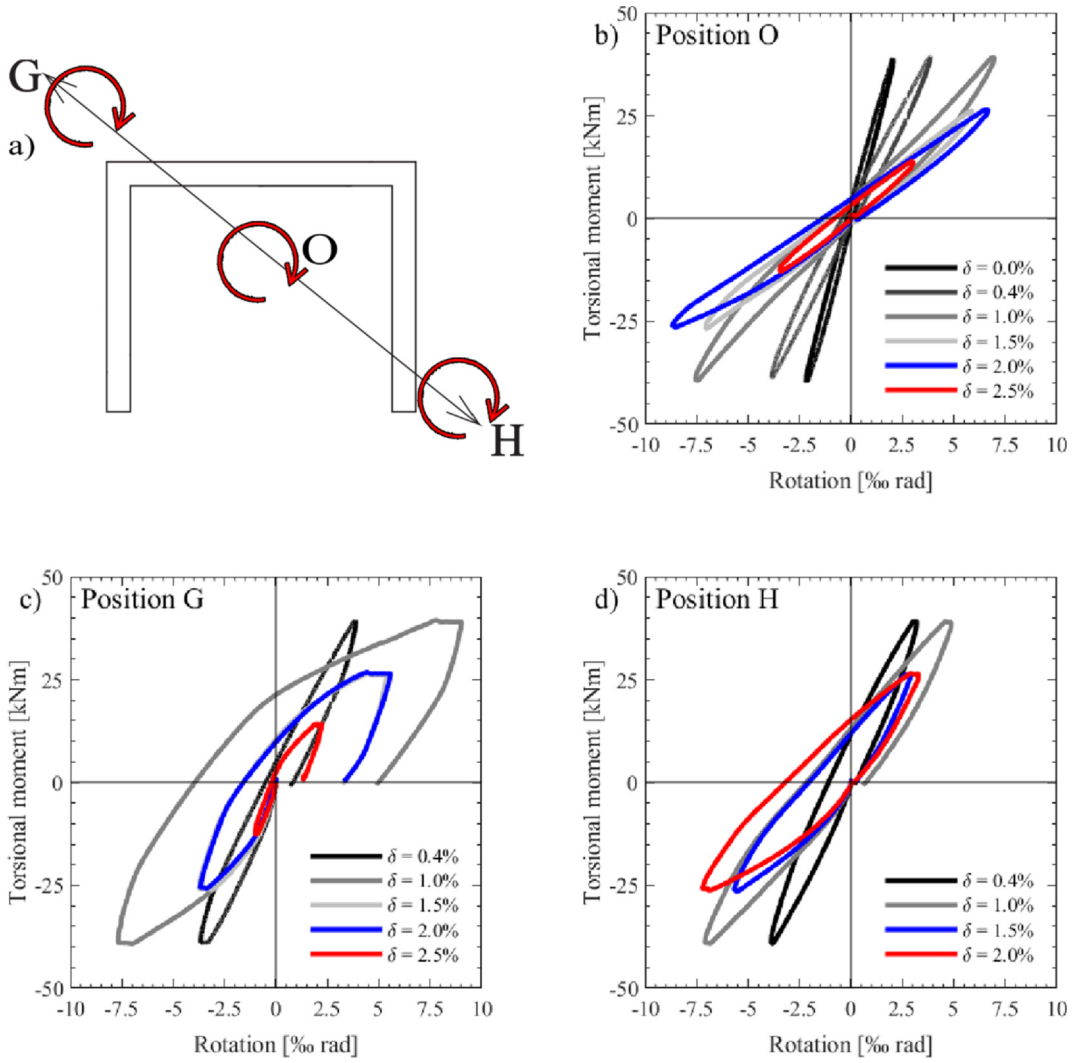


**Fig. 19.** Specimen TUF: (a) positions of the wall at which the twist was applied and Torque-Rotation results at (b) position O (c) position G and (d) position H.

**Table 5**
Specimen TUF: rotational (torsional) stiffness values determined experimentally (in kNm/mrad).

| Position | Ductility ($\mu$) [and $\delta$ (%)] | | | | | |
|---|---|---|---|---|---|---|
| | 0.00 [0.0%] | 0.45 [0.4%] | 1.13 [1.0%] | 1.69 [1.5%] | 2.26 [2.0%] | 2.82 [2.5%] |
| O | 18.7 | 10.1 | 5.4 | 4.1 | 3.4 | 4.1 |
| G | – | 10.4 | 4.7 | 5.8 | 5.7 | 8.3 |
| H | – | 11.1 | 6.5 | 6.2 | 5.0 | – |

Overall, the decay in torsional stiffness follows the decay in translational stiffness. These results substantiate the theory that the decay in torsional stiffness at position O, when the wall is not subjected to any translational displacements (Fig. 20a), is greater in comparison to the wall loaded at a translational displacement, such as that at positions G and H (Fig. 20b). These trends correspond to the findings in Hoult and Beyer [32], where the walls that were investigated were loaded along their principal axes. Hence, the decay of the torsional stiffness for loading in the diagonal direction is similar for loading along the principal axes. For a more in-depth discussion on the decay of the torsional stiffness the reader is therefore referred to Hoult and Beyer [32].

## 5. Conclusions

This paper presented results from the experimental tests of two slender RC U-shaped walls with a single layer of vertical reinforcement. The walls were subjected to quasi-static loading in (i) the in-plane directions for specimen TUE and (ii) the diagonal directions for specimen TUF. One of the primary objectives of the tests was to observe if out-of-plane instability is an issue for these types of walls. The following is a summary of some of the experimental observations and measurements undertaken here for these two U-shaped wall specimens:

- Local out-of-plane buckling was observed in the boundary end regions of both flanges and for both test specimens. This behavior is largely due to the unrestrained lumped longitudinal reinforcing bars at the ends of the flanges, which had diameters almost three times greater than those of the evenly distributed rebars, as well as the chosen loading protocols of the walls. This type of failure was determined to be a localized failure following the criterion given in Dashti et al. [21], where only a small degradation of strength was associated with this secondary mode of failure. For TUE and TUF, local out-of-plane buckling led to a reduction of strength of about 45% and 30%, respectively. For this reason, in conjunction with limiting the drifts in the direction that would cause large compression strains to the buckled regions of the walls, testing was continued.

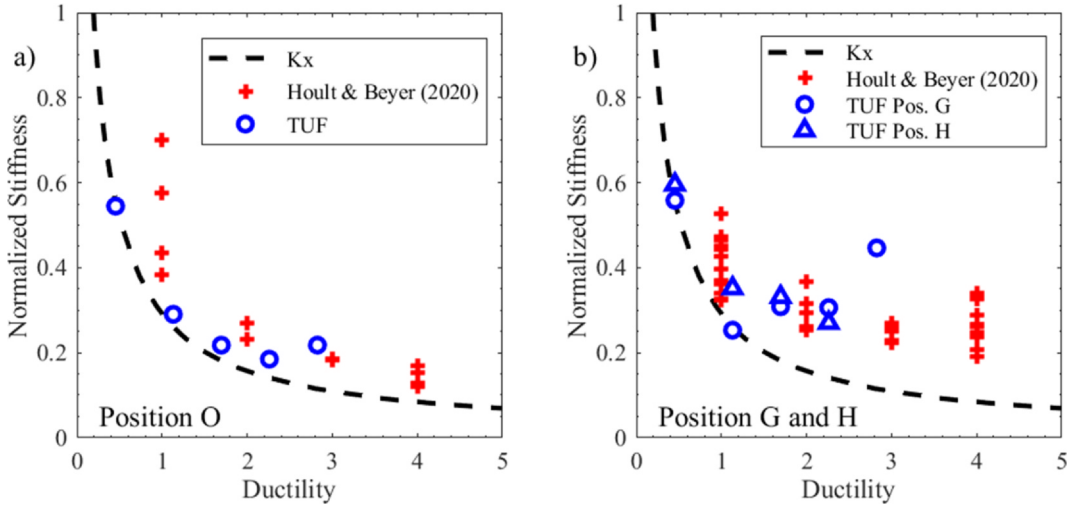


**Fig. 20.** Normalized rotational stiffness results compared to the normalized translational stiffness ($K_x$) for (a) position O and (b) positions G and H.

- Both specimens eventually failed due to concrete crushing in the corners of the web-flange intersections. Shear sliding was also observed for both specimens, predominantly though for specimen TUE with in-plane loading in the direction parallel to the web. It is emphasized that the drifts during testing were limited in the direction where the flexural and shear actions of the wall would produce large longitudinal compression strains in the boundary ends of the wall. Thus, it is possible that global failure could have occurred in these regions and at an earlier drift level than what was observed.
- The displacement profiles of the boundary end of the flanges loaded in tension or compression activated mostly the entire flange, reaching out-of-plane displacements of 10–15% of the wall thickness. However, these out-of-plane displacements were not sufficient to trigger a global out-of-plane failure mode. Furthermore, it was found that the largest out-of-plane deformations for each cycle did not necessarily coincide with an imposed 0% drift (i.e., at position O), which contrasts with the findings in Rosso et al. [49] for mostly planar walls. However, it should be noted that these local out-of-plane buckling failures were observed to occur, in most cases, when the wall was approximately centered.
- Using the expressions from Paulay and Priestley [44], one obtains an out-of-plane displacement of $0.12t_w$ for specimen TUE as a threshold for the onset of out-of-plane instability, which appeared to be a reasonable approximation in comparison to the LED data prior to the local failure observed.
- A small twist was subjected to specimen TUF when the wall was centered and for two diagonal directions to determine the torsional stiffness as a function of drift. The results indicated that when the wall is centered the rate of decay of torsional stiffness is equivalent to the rate of decay of translational stiffness of the wall. However, when the wall is at a translational (i.e., diagonal) position, the rate of decay of torsional stiffness is less than the rate of decay of translational stiffness, substantiating previous numerical and experimental investigations [32].

Given the results from these tests, the following conclusions could be made concerning the seismic behavior of slender RC U-shaped walls with a single-layer of longitudinal reinforcement:

- The loading protocol used for the two wall specimens studied here has shown that local out-of-plane instability can be a problem for these types of walls. A wall with a single-layer of reinforcement has been known to be more susceptible to out-of-plane deformations, and to occur at a lower critical tensile strain, in comparison to walls detailed with two layers of longitudinal reinforcement [44]. Interestingly, the boundary ends of the walls here, unconfined and detailed with a single-layer, appeared to buckle before the concrete had crushed, as clearly shown in the attached video (see Video 1 online). However, as a large reduction of strength was not observed, and the buckling length was limited to the presumed yielding length of the boundary ends, these were determined to be “local” failures. Thus, while it has been known that non-planar walls exacerbate the out-of-plane instability behavior [53], it appears that this type of behavior is restricted to some length above the base (i.e., most likely the yielding length of the wall), rather than a global out-of-plane failure of the entire wall height. It is possible that the web of the wall provides some constraint of the flanges to restrict them from a global out-of-plane-type failure mode. Thus, unconfined and singly-reinforced non-planar walls appear to be more susceptible to failure due to the concrete crushing. However, numerical research, using state-of-the-art finite element modelling, is being proposed by the authors, using the experimental results here to calibrate the models, where a parametric study will be undertaken to better understand the different parameters that can worsen the effect of out-of-plane instability of these types of walls.
- Crushing in the corners of the wall emphasizes the importance of confinement in the critical regions of the wall, such as the boundary ends of the flanges and the web-flange intersection regions. However, this cannot be achieved in slender walls (i.e., thin) with a single layer of vertical reinforcement, which is the current construction practice in Colombia and other Latin American countries. A recent analysis of nine buildings located in Cali, a high seismic region of Colombia, showed that 90% of the walls were detailed with a single layer of reinforcement and 30% had a thickness less than or equal to 100 mm, where the maximum thickness was 150 mm [48].

The experimental data compiled from these two tests will be made publicly available (see Section 6) and will complement the limited database of non-rectangular and singularly reinforced concrete walls. It is hoped that this data will be used to further validate future numerical models. Future research pursuits by the authors including analyzing the DIC data, which will provide further invaluable information on the seismic performance of these types of walls.

## 6. Numerical data and reproducibility

The experimental and numerical dataset from the numerical research investigation undertaken in this paper can be downloaded from the publicly accessible platform Zenodo, DOI: https://doi.org//

10.5281/zenodo.3614079. The structure of the data folders is described in the report 'Data_organization_Hoult_et_al_2020.pdf', also available for download. The following data is provided: (1) experimental dataset for specimens TUE and TUF (2) MATLAB files for reading the data, and (3) MATLAB files for reproducing graphs and figures. This readily available dataset allows transparency of the data and files that were used to compile the results in this paper. Furthermore, the dataset also allows reproducibility studies to be conducted with some ease. The dataset also allows greater opportunities for sharing and reusing the research data produced from this investigation, which may help future studies focusing on similar topics.

## CRediT authorship contribution statement

**Ryan Hoult:** Conceptualization, Methodology, Software, Validation, Investigation, Data curation, Writing - original draft. **Aaron Appelle:** Conceptualization, Methodology, Software, Validation, Investigation, Data curation, Writing - review & editing. **João Almeida:** Conceptualization, Validation, Writing - review & editing, Funding acquisition. **Katrin Beyer:** Conceptualization, Validation, Writing - review & editing, Supervision, Project administration.

## Declaration of Competing Interest

The authors declare that they have no known competing financial interests or personal relationships that could have appeared to influence the work reported in this paper.

## Acknowledgements

The authors would like to acknowledge the support of the Swiss Government Excellence Postdoctoral Scholarship for the year 2018/2019, the Fulbright US Student Program, and the funding provided through the Swiss Bilateral Research Programs for the Latin American Region through the one-year research merger scheme. The authors would also like to thank our partners from Colombia, including Carlos Blandón Uribe from Universidad EIA, Carlos Arteta and Gustavo Rodriguez from Universidad del Norte, Ricardo Bonett from Universidad de Medellín, Ana B. Acevedo Jaramillo from Universidad EAFIT, and Mario E. Rodriguez from Universidad Nacional Autónoma de México.

## Appendix A. Supplementary data

Supplementary data to this article can be found online at https://doi.org/10.1016/j.engstruct.2020.111257.

## References

[1] Albidah A. Vulnerability and Risks of Collapse of Structural Concrete Walls in Regions of Low to Moderate Seismicity. Australia: (Doctor of Philosophy), The University of Melbourne; 2016.
[2] Almeida J, Prodan O, Rosso A, Beyer K. Tests on Thin Reinforced Concrete Walls Subjected to In-Plane and Out-of-Plane Cyclic Loading. Earthquake Spectra 2017;33(1):323–45. https://doi.org/10.1193/101915eqs154dp.
[3] Altheeb A. Seismic Drift Capacity of Lightly Reinforced Concrete Shear Walls. Doctor of Philosophy. Australia: The University of Melbourne; 2016.
[4] Arteta, C., Sánchez, J., Daza, R., Blandón, C., Bonett, R., Carrillo, J., and Vélez, J. (2017). Global and local demand limits of thin reinforced concrete structural wall building systems. Paper presented at the 16th world conference on earthquake engineering. Santiago, Chile.
[5] Behrouzi, A., Mock, A., Lehman, D., Lowes, L., and Kuchma, D. (2018). Seismic Performance of Slender C-shaped Walls Subjected to Uni- and Bi-directional Loading. Paper presented at the Eleventh U.S. National Conference on Earthquake Engineering, Losa Angeles, California.
[6] Belletti B, Damoni C, Gasperi A. Modeling approaches suitable for pushover analyses of RC structural wall buildings. Eng Struct 2013;57:327–38. https://doi.org/10.1016/j.engstruct.2013.09.023.
[7] Beyer K, Dazio A, Priestley MJN. Inelastic Wide-Column Models for U-Shaped Reinforced Concrete Walls. J Earthquake Eng 2008;12(sup1):1–33. https://doi.org/10.1080/13632460801922571.
[8] Beyer K, Dazio A, Priestley MJN. Quasi-Static Cyclic Tests of Two U-Shaped Reinforced Concrete Walls. J Earthquake Eng 2008;12(7):1023–53. https://doi.org/10.1080/13632460802003272.
[9] Beyer K, Dazio A, Priestley MJN. Shear Deformations of Slender Reinforced Concrete Walls under Seismic Loading. ACI Struct J 2011;108(2):167–77.
[10] Beyer K, Dazio A, Priestley N. Quasi-Static Cyclic Tests of Two U-Shaped Reinforced Concrete Walls. 2015.
[11] Beyer, K., Hube, M., Constantin, R., Niroomandi, A., Pampanin, S., Dhakal, R., Sritharan, S., Wallace, J. (2017). Reinforced concrete wall response under uni-and bi-directional loading. Proc. of the 16th World Conference on Earthquake Engineering, Santiago, Chile, 2017.
[12] Blandón C, Bonett R. Thin slender concrete rectangular walls in moderate seismic regions with a single reinforcement layer. Journal of Building Engineering 2020;28:101035https://doi.org/10.1016/j.jobe.2019.101035.
[13] Blandón CA, Arteta CA, Bonett RL, Carrillo J, Beyer K, Almeida JP. Response of thin lightly-reinforced concrete walls under cyclic loading. Eng Struct 2018;176:175–87. https://doi.org/10.1016/j.engstruct.2018.08.089.
[14] Carrillo J, Alcocer SM. Seismic performance of concrete walls for housing subjected to shaking table excitations. Eng Struct 2012;41:98–107. https://doi.org/10.1016/j.engstruct.2012.03.025.
[15] CEN. (2004). Eurocode 8: Design of structures for earthquake resistance. Part 1: general rules, seismic actions and rules for buildings. In E. S. E. 1998-1:2004 (Ed.). In. Brussels, Belgium, 2004: Comit´e Europ´een de Normalisation.
[16] Chai YH, Elayer DT. Lateral Stability of Reinforced Concrete Columns under Axial Reversed Cyclic Tension and Compression. Structural Journal 1999;96(5). https://doi.org/10.14359/732.
[17] Constantin, R., and Beyer, K. (2014). Non-rectangular RC walls: A review of experimental investigations. Paper presented at the 2nd European Conference on Earthquake Engineering and Seismology, Istanbul, Turkey.
[18] Constantin R, Beyer K. Behaviour of U-shaped RC walls under quasi-static cyclic diagonal loading. Eng Struct 2016;106:36–52. https://doi.org/10.1016/j.engstruct.2015.10.018.
[19] Solutions C. VIC-3D (Version 7) Retrieved from http://www.correlatedsolutions.com; 2019.
[20] Dashti F, Dhakal RP, Pampanin S. Evolution of out-of-plane deformation and subsequent instability in rectangular RC walls under in-plane cyclic loading: Experimental observation. 2018;47(15):2944–64. https://doi.org/10.1002/eqe.3115.
[21] Dashti F, Dhakal RP, Pampanin S. Out-of-Plane Response of In-Plane-Loaded Ductile Structural Walls: State-of-the-Art and Classification of the Observed Mechanisms. J Earthquake Eng 2020;1–22. https://doi.org/10.1080/13632469.2020.1713928.
[22] Dazio A, Beyer K, Bachmann H. Quasi-static cyclic tests and plastic hinge analysis of RC structural walls. Eng Struct 2009;31(7):1556–71. https://doi.org/10.1016/j.engstruct.2009.02.018.
[23] ElMohandes F, Vecchio F. Vector3 and FormWorks Plus User Manual. Department of Civil Engineering: University of Toronto; 2013. Retrieved from http://www.civ.utoronto.ca/vector/user_manuals/manual6.pdf.
[24] Goodsir WJ. The design of coupled frame-wall structures for seismic actions (Ph.D.). Christchurch, New Zealand: University of Canterbury; 1985.
[25] Haro AG, Kowalsky M, Chai YH, Lucier GW. Boundary Elements of Special Reinforced Concrete Walls Tested under Different Loading Paths. Earthquake Spectra 2018;34(3):1267–88. https://doi.org/10.1193/081617eqs160m.
[26] Hines EM, Dazio A, Chou CC, Seible F. *Structural testing of the San Francisco-Oakland bay bridge east span skyway piers* (Technical Report SSRP-2002/1). California, USA: Retrieved from La Jolla; 2002.
[27] Hoult, R. D., Lumantarna, E., and Goldsworthy, H. M. (2015a). Torsional Displacement for Asymmetric Low-Rise Buildings with RC C-shaped Cores. Paper presented at the Proceedings of the Tenth Pacific Conference on Earthquake Engineering, Sydney, Australia.
[28] Hoult, R. D., Goldsworthy, H. M., and Lumantarna, E. (2015b). Improvements and difficulties associated with the seismic assessment of infrastructure in Australia. Paper presented at the Australasian Fire and Emergency Service Authorities Council (AFAC) 2015 conference, Adelaide, South Australia.
[29] Hoult R, Goldsworthy H, Lumantarna E. Plastic Hinge Length for Lightly Reinforced Rectangular Concrete Walls. J Earthquake Eng 2018;22(8):1447–78. https://doi.org/10.1080/13632469.2017.1286619.
[30] Hoult R, Goldsworthy HM, Lumantarna E. Plastic Hinge Length for Lightly Reinforced C-shaped Concrete Walls. J Earthquake Eng 2018;1–32. https://doi.org/10.1080/13632469.2018.1453419.
[31] Hoult RD. Shear Lag Effects in Reinforced Concrete C-shaped Walls. J Struct Eng 2019;145(3):04018270. https://doi.org/10.1061/(ASCE)ST.1943-541X.0002272.
[32] Hoult RD, Beyer K. Decay of Torsional Stiffness of RC U-shaped Walls When Subjected Simultaneously to In-plane Translational Displacements. J Struct Eng 2020;146(9). https://doi.org/10.1061/(ASCE)ST.1943-541X.0002733.
[33] Hube MA, María HS, Arroyo O, Vargas A, Almeida J, López M. Seismic performance of squat thin reinforced concrete walls for low-rise constructions. Earthquake Spectra 2020. https://doi.org/10.1177/8755293020906841.
[34] Ile N, Reynouard JM. Behaviour of U-shaped Walls Subjected to Uniaxial and Biaxial Cyclic Lateral Loading. J Earthquake Eng 2005;09(01):67–94.
[35] Krolicki J, Maffei J, Calvi GM. Shear Strength of Reinforced Concrete Walls Subjected to Cyclic Loading. J Earthquake Eng 2011;15(sup1):30–71. https://doi.org/10.1080/13632469.2011.562049.
[36] Lu Y, Henry RS. Comparison of Minimum Vertical Reinforcement Requirements for Reinforced Concrete Walls. ACI Struct J 2018;115(3). https://doi.org/10.14359/51701146.

[37] Maffei, J., Bonelli, P., Kelly, D., Lehman, D. E., Lowes, L., Moehle, J., . . . Willford, M. (2014). Recommendations for seismic design of reinforced concrete wall buildings based on studies of the 2010 Maule, Chile earthquake.
[38] Massone LM, Bonelli P, Lagos R, Lüders C, Moehle J, Wallace JW. Seismic design and construction practices for RC structural wall buildings. Earthquake Spectra 2012;28(S1):S245–56.
[39] Menegon SJ, Wilson JL, Lam NTK, Gad EF. Experimental Testing of Nonductile Reinforced Concrete Wall Boundary Elements. ACI Struct J 2019;116(6). https://doi.org/10.14359/51718008.
[40] NDI. (2010). Optotrak Certus HD. Technical report. Retrieved from Northern Digital Inc. Waterloo, Ontario (Canada): http://www.ndigital.com/industrial/certushd.php.
[41] Oesterle RG, Fiorato AE, Johal LS, Carpenter JE, Russell HG, Corley WG. Earthquake Resistant Structural Walls - Tests of Isolated Walls. Illinois: Retrieved from Skokie; 1976.
[42] Parra PF, Moehle JP. Stability of Slender Wall Boundaries Subjected to Earthquake Loading. Structural Journal 2017;114(6). https://doi.org/10.14359/516851700836.
[43] Paulay, T., and Priestley, M. J. N. (1992). Seismic design of reinforced concrete and masonry buildings / T. Paulay, M.J.N. Priestley: New York : Wiley, c1992.
[44] Paulay T, Priestley MJN. Stability of Ductile Structural Walls. Structural Journal 1993;90(4). https://doi.org/10.14359/3958.
[45] Pelletier K, Léger P. Nonlinear seismic modeling of reinforced concrete cores including torsion. Eng Struct 2017;136:380–92. https://doi.org/10.1016/j.engstruct.2017.01.042.
[46] Peng X-N, Wong Y-L. Behavior of reinforced concrete walls subjected to monotonic pure torsion—An experimental study. Eng Struct 2011;33(9):2495–508. https://doi.org/10.1016/j.engstruct.2011.04.022.
[47] Puranam, A., and Pujol, S. (2017). Minimum Flexural Reinforcement in Reinforced Concrete Walls. Paper presented at the 16th World Conference on Earthquake Engineering, Santiago, Chile.
[48] Rosso, A. (2018). Out-of-plane instability of thin reinforced concrete walls under seismic loading. (Ph.D.), École polytechnique fédérale de Lausanne, Lausanne, Swizterland. (8413).
[49] Rosso A, Almeida JP, Beyer K. Stability of thin reinforced concrete walls under cyclic loads: state-of-the-art and new experimental findings. Bull Earthq Eng 2016;14(2):455–84. https://doi.org/10.1007/s10518-015-9827-x.
[50] Rosso A, Jiménez-Roa LA, Almeida JPD, Zuniga APG, Blandón CA, Bonett RL, Beyer K. Cyclic tensile-compressive tests on thin concrete boundary elements with a single layer of reinforcement prone to out-of-plane instability. Bull Earthq Eng 2018;16(2):859–87.
[51] Smyrou E, Sullivan T, Priestley N, Calvi M. Sectional response of T-shaped RC walls. Bull Earthq Eng 2013;11(4):999–1019. https://doi.org/10.1007/s10518-012-9407-2.
[52] Sritharan S, Beyer K, Henry RS, Chai YH, Kowalsky M, Bull D. Understanding Poor Seismic Performance of Concrete Walls and Design Implications. Earthquake Spectra 2014;30(1):307–34. https://doi.org/10.1193/021713EQS036M.
[53] Thomsen J, Wallace J. Displacement-Based Design of Slender Reinforced Concrete Structural Walls—Experimental Verification. J Struct Eng 2004;130(4):618–30. https://doi.org/10.1061/(ASCE)0733-9445(2004)130:4(618).
[54] Tripathi M, Dhakal RP, Dashti F, Massone LM. Low-cycle fatigue behaviour of reinforcing bars including the effect of inelastic buckling. Constr Build Mater 2018;190:1226–35. https://doi.org/10.1016/j.conbuildmat.2018.09.192.